AGU PUBLICATIONS

Geochemistry, Geophysics, Geosystems

RESEARCH ARTICLE
10.1002/2014GC005554

Effects of crystal shape- and size-modality on magma rheology

P. Moitra[1] and H. M. Gonnermann[1]

[1]Department of Earth Sciences, Rice University, Houston, Texas, USA

Key Points:
- Analog rheology experiments dynamically similar to crystalline magma performed
- Maximum packing is the key parameter governing crystal-rich magma rheology
- Crystalline magma ascent rates with Herschel-Bulkley rheology is estimated

Correspondence to:
P. Moitra,
Pranabendu.moitra@rice.edu

Citation:
Moitra, P., and H. M. Gonnermann (2015), Effects of crystal shape- and size-modality on magma rheology, *Geochem. Geophys. Geosyst.*, *16*, doi:10.1002/2014GC005554.

Received 22 AUG 2014
Accepted 25 NOV 2014
Accepted article online 4 DEC 2014

Abstract Erupting magma often contains crystals over a wide range of sizes and shapes, potentially affecting magma viscosity over many orders of magnitude. A robust relation between viscosity and the modality of crystal sizes and shapes remains lacking, principally because of the dimensional complexity and size of the governing parameter space. We have performed a suite of shear viscosity measurements on liquid-particle suspensions of dynamical similarity to crystal-bearing magma. Our experiments encompass five suspension types, each consisting of unique mixtures of two different particle sizes and shapes. The experiments span two orthogonal subspaces of particle concentration, as well as particle size and shape for each suspension type, thereby providing insight into the topology of parameter space. For each suspension type, we determined the dry maximum packing fraction and measured shear rates across a range of applied shear stresses. The results were fitted using a Herschel-Bulkley model and augment existing predictive capabilities. We demonstrate that our results are consistent with previous work, including friction-based constitutive laws for granular materials. We conclude that predictions for ascent rates of crystal-rich magmas must take the shear-rate dependence of viscosity into account. Shear-rate dependence depends first and foremost on the volume fraction of crystals, relative to the maximum packing fraction, which in turn depends on crystal size and shape distribution.

1. Introduction

Characterizing the effect of crystals on magma rheology is a necessary requirement to understand and estimate magma flow in a range of magmatic processes, such as in magma chambers [e.g., *Bachmann and Bergantz*, 2003; *Sparks*, 2003; *Karlstrom et al*., 2010; *Hodge et al*., 2012; *Huber et al*., 2012], magma flow through dikes and volcanic conduits [e.g., *Melnik and Sparks*, 1999; *Moitra et al*., 2013], and lava flows [e.g., *Cashman et al*., 1999; *Hoover et al*., 2001; *Chevrel et al*., 2013; *Castruccio et al*., 2014]. Although the viscosity of silicate melts is a function of composition, temperature, and water content [e.g., *Webb and Dingwell*, 1990; *Zhang et al*., 2007; *Giordano et al*., 2008], the deformational response of magma to an applied stress can also be significantly modulated by the presence of bubbles or crystals [e.g., *McBirney and Murase*, 1984; *Kerr and Lister*, 1991; *Pinkerton and Stevenson*, 1992; *Lejeune and Richet*, 1995; *Manga et al*., 1998; *Rust et al*., 2003; *Llewellin and Manga*, 2005; *Caricchi et al*., 2007; *Ishibashi and Sato*, 2007; *Lavallèe et al*., 2007; *Champallier et al*., 2008; *Sumita and Manga*, 2008; *Costa et al*., 2009; *Petford*, 2009; *Vona et al*., 2011; *Cimarelli et al*., 2011; *Mueller et al*., 2011; *Pistone et al*., 2012; *Del Gaudio et al*., 2013; *Mader et al*., 2013; *Picard et al*., 2013]. The work described herein investigates the rheological properties (the deformational response to an applied stress) of particle-liquid suspensions that are dynamically analogous to crystal-bearing magmas.

The effect of crystals on the flow of magma depends on the concentration as well as the shape and size distribution of crystals, with a wide range observable in igneous rocks [e.g., *Cashman and Marsh*, 1988; *Marsh*, 1988, 1998; *Higgins*, 2000, 2006; *Jerram and Martin*, 2008]. For example, the ongoing eruption of Soufrière Hills volcano has been characterized by the eruption of highly crystalline magma at variable rates and it is punctuated by pauses in the eruption *Sparks et al*., 1998. Crystals span a wide range in shape [*Higgins and Roberge*, 2003] and in size, often exhibiting a strong bimodal distribution (Figure 1) [*Giachetti et al*., 2010], and it is thought that the crystals have a significant effect on magma extrusion rate [*Melnik and Sparks*, 1999, 2002].

The wide range in crystal size and shape found in magmas therefore provides an unambiguous incentive to improve our understanding of how crystal shape and size distributions affect the deformational behavior of magmas and, hence, their eruption styles. The objective of this study is to enhance the constitutive laws for magma with crystals of different distributions in size and shape. A convenient way of achieving this

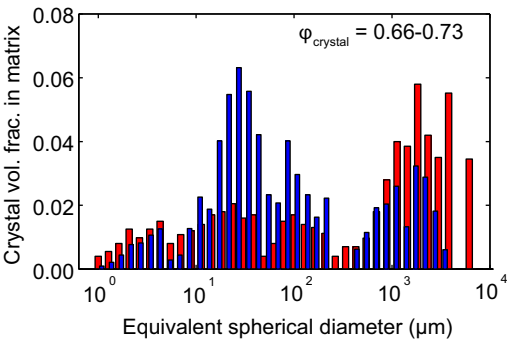

Figure 1. Example of two crystal size distribution in two pyroclasts (sample ID s AMO29 and R2) from the 1997 Vulcanian explosions of Soufrière Hills Volcano (modified from *Giachetti et al*. [2010]). AMO29 is a dense pyroclastic flow pumice and R2 is a fallout pumice, as described in *Giachetti et al*. [2010]. The crystal volume fraction within the solid matrix of glass plus crystals is shown as a function of equivalent spherical diameter of crystals. The total crystal volume fraction, $\phi_{crystal}$ is approximately 0.66-0.73.

objective is through experiments that have dynamic similarity to magmatic conditions, but use materials that are amenable to laboratory conditions at room temperatures and lower stresses than magmas [*Mader et al*., 2004].

Here we present results from such analog experiments focused on liquid-solid suspension with bimodal distributions of particles. A number of studies have already focused on the rheological behavior of bimodal and polymodal size distributions of spherical particles [e.g., *Farris*, 1968; *Chang and Powell*, 1993, 1994; *Chong et al*., 1971; *Shapiro and Probstein*, 1992; *Probstein et al*., 1994; *He and Ekere*, 2001; *Qi and Tanner*, 2011]. Other studies have examined suspensions of nonspherical particles, for example, *Castruccio et al*. [2010] performed experiments with suspensions of cubic shaped sugar crystals of both unimodal and bimodal size distributions.

A few studies have examined mixtures of both different particle size and shape [e.g., *Marti et al*., 2005; *Cimarelli et al*., 2011; *Del Gaudio*, 2014]. For example, *Marti et al*. [2005] worked with mixtures of spheres and fibers of comparable diameter, proposing that the effect on viscosity can be estimated using the theoretical formulations of *Farris* [1968]. In contrast, experiments by *Cimarelli et al*. [2011] were focused on the effect of increasing fraction of microlites in a phenocryst-bearing magma, whereas *Del Gaudio* [2014] examined the effect of particles of arbitrary shapes. Both *Cimarelli et al*. [2011] and *Del Gaudio* [2014] found that the apparent viscosity of their bimodal suspensions can be estimated using the equations of *Costa et al*. [2009], albeit with no clear systematic results on fitting parameters.

Here we aim to build upon this existing body of work, in order to further examine potential functional relationships between the different parameters that define suspension characteristics and their flow behavior. We also use our empirical results to examine their implications for magma ascent within volcanic conduits during eruptions.

2. Overview of Rheological Models

2.1. Relative Viscosity

At any instant, the ratio of shear stress to shear rate defines the shear viscosity of a fluid. The viscosity of a fluid usually increases if particles are added in suspension. This change in viscosity is expressed as the ratio of the viscosity of the suspension (liquid + particle) η_s, to the viscosity of liquid η_l, and is called the relative viscosity η_r. Because of the complicated theory behind multibody particle-particle-liquid interactions, the notion of suspension viscosity, which is based on a continuum approximation, has been proven useful for a wide range of applications [e.g., *Coussot and Ancey*, 1999; *Stickel and Powell*, 2005; *Chhabra and Richardson*, 2011].

The relationship between an applied stress and resultant deformation rate is a manifestation of the aforementioned interactions, and it is the principal macroscopically accessible observation amenable to quantitative measurement. It is therefore of fundamental importance for any field of study involving liquid-particle suspensions. The estimation of suspension viscosity is based on well-established methodologies that yield reproducible direct measurements of shear stress and shear rate using sophisticated rheometers [e.g., *Mezger*, 2006]. Measuring the viscosity of suspensions is also complicated because the relationship between shear stress and shear rate may depend on the shear rate, $\dot{\gamma}$, and also on strain, γ. Therefore, the measured viscosity at any given shear rate and strain is called the apparent viscosity.

A number of models have been proposed to estimate the rheological properties of unimodal particulate suspensions (Table 1). In the pioneering work by *Einstein* [1906], η_r has been expressed as a function of particle volume fraction, ϕ, given by

Table 1. Rheology Models for Liquid-Particle Suspensions

Model	Reference
Apparent Viscosity/Consistency	
$\eta_r = 1 + B\phi$	*Einstein* [1906]
$\eta_r = \left(1 - \frac{\phi}{\phi_m}\right)^{-2}$	*Maron and Pierce* [1956]
$\eta_r = \left(1 - \frac{\phi}{\phi_m}\right)^{-B\phi_m}$	*Krieger and Dougherty* [1959]
$\eta_r = (1+\phi^\delta)/(1-F)^{B\phi_*}$, $F = (1-\zeta)\mathrm{erf}\left[\frac{\sqrt{\pi}}{2(1-\zeta)}\varphi(1+\varphi^\gamma)\right]$	*Costa et al.* [2009]
$\eta_r = \left(1 + 0.75\frac{\phi/\phi_m}{1-\phi/\phi_m}\right)^2$	*Chong et al.* [1971]
$\eta_r = 1 + \frac{3\pi}{8}\frac{\beta}{\beta+1}\left(\frac{3+4.5\beta+\beta^2}{\beta+1} - \frac{3\beta+3}{\beta}\ln(\beta+1)\right)$, $\beta = \frac{(\phi/\phi_m)^{1/3}}{1-(\phi/\phi_m)^{1/3}}$	*Shapiro and Probstein* [1992]
$\eta_r = (\eta_f/\eta_l)(\eta_s/\eta_f)$	*Farris* [1968]
$\eta_r = \left(1 - \frac{\phi}{\phi_m}\right)^{-\alpha}$	This study
Flow Index	
$n = 1 - 2\alpha\left[\ln\left(1 - \frac{\phi}{\phi_m}\right)\right]^2$	*Ishibashi* [2009], *Vona et al.* [2011]
$n = 1 - 0.2r_p\left(\frac{\phi}{\phi_m}\right)^4$	*Mueller et al.* [2010]
$n = 1 + 2\alpha\log\left(1 - \frac{\phi}{\phi_m}\right)$	*Vona et al.* [2011]
$n = 1 - (1 - n_{\min})\left(\frac{\phi}{\phi_{\max}}\right)^{2.3}$	This study
Yield Stress	
$\tau_y = 200\left(\frac{D_p}{\phi_m - \phi}\right)\left(\frac{\phi_m}{1-\phi_m}\right)^2\left(\frac{1}{\xi^{1.5}\sigma_g^2}\right)$,	*Gay et al.* [1969]
$\tau_y = A\left(\frac{\phi/\phi_c - 1}{1-\phi/\phi_m}\right)^{1/p}$	*Wildemuth and Williams* [1984, 1985]
$\tau_y = 6500\phi^{2.85}$	*Ryerson et al.* [1988]
$\tau_y = 5e^6(\phi - \phi_c)^8$	*Castruccio et al.* [2010]
$\tau_y = \tau^*\left[\left(1 - \frac{\phi}{\phi_m}\right)^{-2} - 1\right]$	*Heymann et al.* [2002]
$\tau_y = \tau^*\left[\left(1 - \frac{\phi}{\phi_m}\right)^{-2} - \left(1 - \frac{\phi_c}{\phi_m}\right)^{-2}\right]$	This study

$$\eta_r = 1 + B\phi, \tag{1}$$

where B is a constant with a value of 2.5 in the case of spheres. The Einstein model is limited to suspensions with $\phi \leq 0.10$ [e.g., *Rutgers*, 1962; *Thomas*, 1965; *Mueller et al.*, 2010]. A widely used semi-empirical model for both dilute and concentrated suspensions was proposed by *Krieger and Dougherty* [1959] and is given by

$$\eta_r = \left(1 - \frac{\phi}{\phi_m}\right)^{-B\phi_m}, \tag{2}$$

where ϕ_m is the maximum packing fraction of particles.

Among the models for bimodal to polymodal suspensions, the model by *Farris* [1968] is based on effective medium theory, where the coarser particles are considered to be suspended in a material with properties equivalent to a mixture of finer particles and suspending liquid. The volume fractions of fine and coarse particles are, respectively, defined as $\phi^f_{\text{Farris}} \equiv v_f/(v_f + v_l)$ and $\phi^c_{\text{Farris}} \equiv v_c/(v_c + v_f + v_l)$, where v_f is the volume of fine particles, v_l is the volume of the suspending liquid, and v_c is the volume of the coarse particles. The viscosity of the suspension with only fine particles, η_f, can be estimated using, for example, the Maron-Pierce or Krieger-Dougherty model for unimodal suspensions. Subsequently, using η_f instead of η_l, the value of η_s can be calculated, also using one of the models for unimodal suspensions (Table 1).

2.2. Herschel-Bulkley Model

The aforementioned models predict suspension viscosity as a function of particle volume fraction, ϕ, but neglect shear-rate dependence [e.g., *Cross*, 1970; *Krieger*, 1972; *Wildemuth and Williams*, 1984, 1985] or yield stress [e.g., *Ryerson et al.*, 1988; *Zhou et al.*, 1995; *Hoover et al.*, 2001; *Saar et al.*, 2001; *Mueller et al.*, 2010; *Cimarelli et al.*, 2011; *Mader et al.*, 2013]. Although, the existence and meaning of yield stress have been issues of debate [*Nguyen and Boger*, 1992; *Barnes*, 1999; *Stickel and Powell*, 2005], measurements of shear stress, τ, as a function of $\dot{\gamma}$, indicate that suspension above some critical volume fraction of particles and at low values of $\dot{\gamma}$ undergo a rheological transition that has been attributed to a change from liquid to solid-like behavior. This transition can be characterized within rheological models as an apparent yield stress parameter, τ_y [*Heymann et al.*, 2002; *Coussot*, 2007; *Heymann and Nuri*, 2007].

A model that accounts for both apparent yield stress and strain-rate dependence is the Herschel-Bulkley model [*Herschel and Bulkley*, 1926]

$$\tau = \tau_y + K\dot{\gamma}^n. \tag{3}$$

Here the relationship between τ and $\dot{\gamma}$ depends on three parameters: (1) the yield stress parameter, τ_y; (2) the consistency, K; and (3) the flow index, n. For a Newtonian liquid, $\tau_y = 0$ and $n = 1$, in which case K is equal to the suspension viscosity η_s (Figure 2). The lower asymptotes in Figure 2 represent the effect of τ_y. In theory, once $\tau > \tau_y$, the suspension starts to deform. In experiments, the measurement of yield stress is often confounded by limitations of accurately measuring sufficiently small values of $\dot{\gamma}$ [e.g., *Barnes*, 1999].

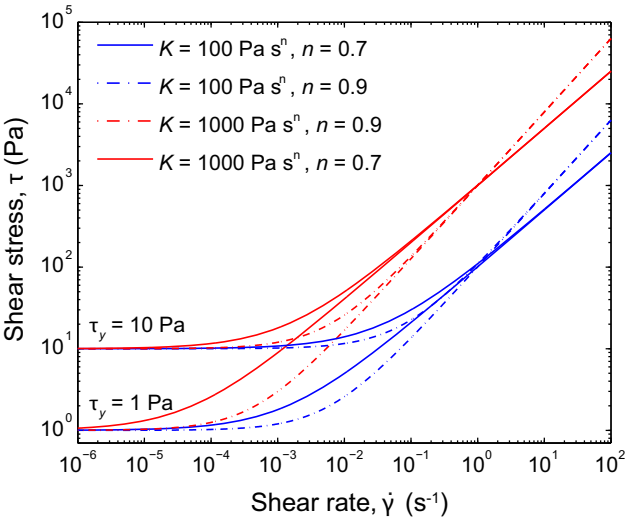

Figure 2. Examples of shear stress, τ, as a function of shear rate, $\dot{\gamma}$ for the Herschel-Bulkley model (equation (3)), illustrating the effects of consistency, *K*, flow index, *n*, and yield stress, τ_y.

The flow index *n* defines the extent of shear-rate dependence, where the slope $d\tau/d\dot{\gamma}$ becomes less steep as *n* decreases. In other words, smaller values of *n* indicate a greater dependence of apparent viscosity on shear rate. To achieve a wide range of applicability for equation (3), we seek for each of these three parameters functional dependences on particle shape, particle size, total volume fraction of particles, and relative proportions of particles with different shape and/or size.

2.3. Maximum Packing Fraction

It has been found that the maximum packing fraction of the particle mixture, ϕ_m, is a key parameter in controlling the rheological response of suspensions [e.g., *Mader et al*., 2013]. The maximum packing fraction, ϕ_m, is the volume fraction of particles required to fill a container. It can be viewed as the critical concentration of particles at which the suspension becomes jammed [e.g., *Liu and Nagel*, 1998; *Song et al*., 2008]. The latter refers to a physical state where an interconnected network of particles renders the suspension nondeformable so that viscosity tends to infinity [e.g., *Krieger and Dougherty*, 1959]. At volume fractions below ϕ_m, the deformation of the suspension involves the flow of liquid in-between particles, which themselves tend to be nonstationary. With increasing volume fraction, ϕ, the average interparticle distance decreases, resulting in larger gradients in interstitial liquid velocity and higher viscosity of the bulk suspension.

ϕ_m depends on the distribution of particle sizes and shapes, as well as the packing geometry [e.g., *McGeary*, 1961; *Milewski*, 1973; *Ouchiyama and Tanaka*, 1981; *Wildemuth and Williams*, 1984; *Sudduth*, 1993; *Yu et al*., 1996; *Torquato et al*., 2000; *Zou et al*., 2003; *Donev et al*., 2004; *Weitz*, 2004; *Bournonville et al*., 2005; *Brouwers*, 2006; *Prior et al*., 2013; *Baule and Makse*, 2014]. For example, for spheres in cubic or in random close packing, $\phi_m \approx 0.52$ or 0.74, respectively; and for random close packing of ellipsoids, $\phi_m \approx 0.74$ (for aspect ratio $\approx$ 1.3) [*Donev et al*., 2004]. Here we are interested in the random close packing of mixtures of particles of different shapes and sizes, seeking a functional relationship of ϕ_m by measuring ϕ_m experimentally for a range of modalities in particle size and shape.

3. Experimental Methods

3.1. Particle Types

We used four different types of particles, each of different size and/or shape (Figure 3 and Table 2). Solid glass spheres of average diameter of 4 and 100 μm (Microspheres-Nanospheres™) were used, denoted as "s" and "S," respectively. For particles of large aspect ratio, we used wollastonite fibers (Fibertech™) of aspect ratio 8 and average length 35 μm, denoted by "e," and glass fibers (Fibertech™) of average aspect ratio 6 and average length 122 μm, denoted by "E."

3.2. Particle Mixtures

Suspensions were comprised of three different particle mixtures: (1) unimodal particles only at varying ϕ; (2) bimodal with a constant volume fraction of smaller or fibrous particles of $\phi_f = 0.25$, but different ϕ; and (3) bimodal with a constant value of $\phi = 0.30$, but with varying ϕ_f (Figure 4a and Table 3). In this study, $\phi = (v_f + v_c)/(v_c + v_f + v_l)$ and $\phi_f = v_f/(v_c + v_f)$. The suspensions were prepared using silicone oil (Brookfield Co.™) of viscosity 102 Pa s as the suspending liquid by mixing and deaerating liquid plus particles using a Kurabo Mazerustar™ planetary mixer. All experiments were performed at a temperature of 25°C and a liquid density of 0.97 g cm^{-3}.

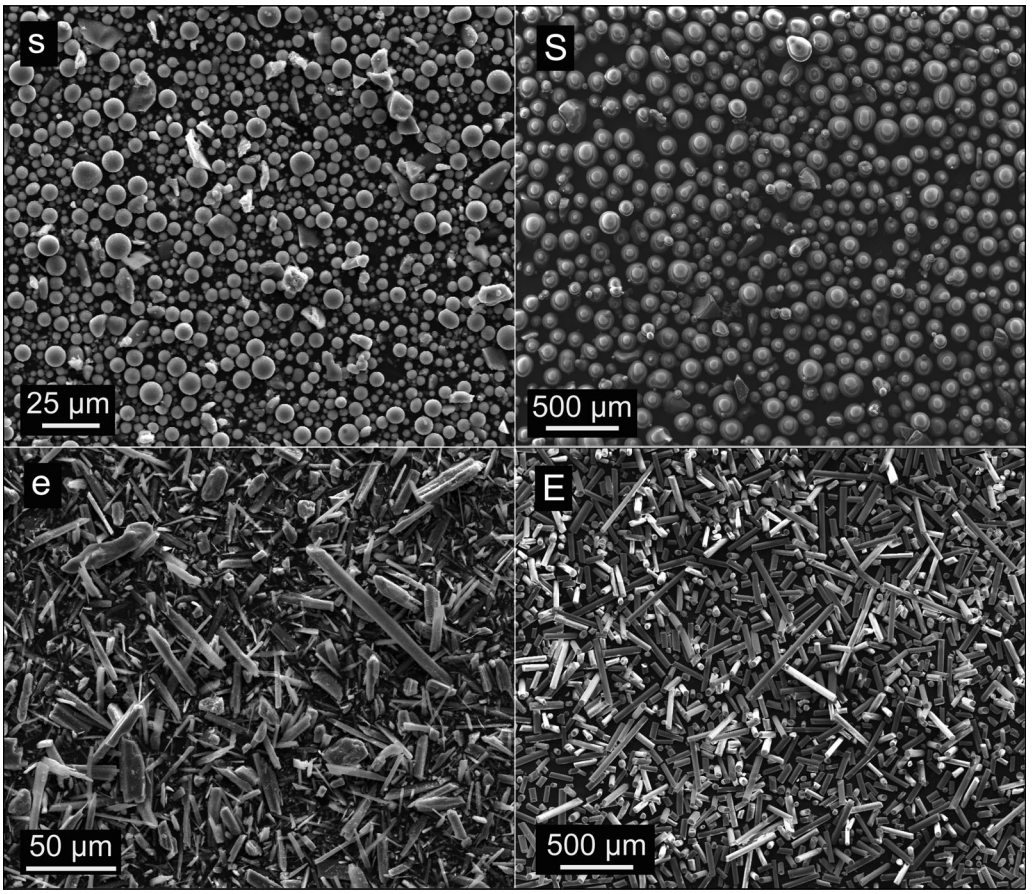

Figure 3. Secondary electron images of the small (s) and large (S) glass spheres, as well as the high aspect ratio wollastonite (e) and glass fibers (E) used in this study. The physical properties of these particles are listed in Table 2.

3.3. Dry Maximum Packing Fraction

The volume of particles prior to packing was obtained by measuring the mass of particles and dividing it by the particle density. The latter was measured using helium pycnometry (AccuPyc II 1340 Pycnometer, Micromeritics Instrument Co.). The volume occupied by the particle mixture in the randomly packed state was then determined using a GeoPyc® 1360 (Micromeritics Instrument Co.) using the T.A.P.™ option, where the particles were consolidated under a force of 20 N within a glass cylinder of known diameter and the height of the particle mixture was measured using a linear displacement sensor (Figure 4b). These measurements

Table 2. Particles Used in the Experiments[a]

	s	S	e	E
Shape	Spherical	Spherical	Cylindrical	Cylindrical
Material	Glass	Glass	Glass	Wollastonite
Diameter range (μm)	2–13	36–172	13–25	2–10
Average diameter (μm)	~4	~100	~20	~5
$\sigma_{diameter}$ (μm)	2	32	2	4
Length range (μm)			23–444	18–106
Average length (μm)			122	35
σ_{length} (μm)			99	18
Aspect ratio range (μm)			2–20	4–13
Average aspect ratio	1	1	~6	~8
$\sigma_{aspectratio}$ (μm)			4	3
Density (gm/cc)	2.5	2.5	2.5	2.9
Peclet number ($\dot{\gamma}=10^{-4}s^{-1}$)	6×10^{3}	2×10^{8}	2×10^{4}	2×10^{6}
Reynolds number ($\dot{\gamma}=1s^{-1}$)	2×10^{-9}	2×10^{-6}	5×10^{-9}	1×10^{-7}
Stokes number ($\dot{\gamma}=1s^{-1}$)	6×10^{-9}	5×10^{-6}	1×10^{-8}	3×10^{-7}

[a] σ is the standard deviation.

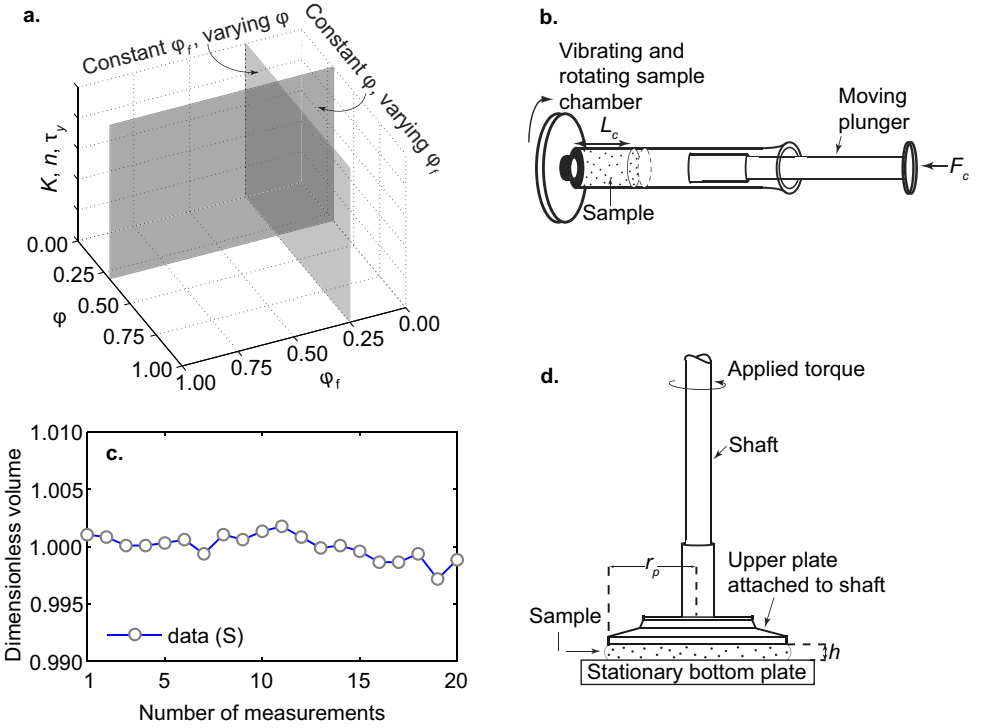

Figure 4. (a) Illustrative diagram of ϕ–ϕ_f parameter space, together with subspaces covered by our experiments. (b) Schematic diagram illustrating the methodology used to determine the maximum packing fraction, ϕ_m, using the tapped density technique. F_c is the applied force and L_c is the measured length after compaction. (c) Example of the measured volume of packed particles divided by the average value of the cylinder volume occupied by the particles, for 20 repeat measurements for particle "S." (d) Schematic diagram of parallel plate geometry used for the shear rheology experiments. r_p is the radius of the upper plate, and h is the gap-width between lower and upper plates.

were performed with 20 pre-measurement cycles and 20 measurement cycles (Figure 4c), and no particle breakage was observed.

3.4. Suspension Characteristics

The rheophysical properties of suspensions, that is, the interaction of forces can be defined by three nondimensional numbers, which are the Peclet number, Pe, the particle Reynolds number, Re_p, and the Stokes number, St (Table 2). They represent, respectively, the relative importance of Brownian, inertial, and hydrodynamic forces during the experiments [e.g., *Coussot and Ancey*, 1999; *Stickel and Powell*, 2005]. All of our experiments are in the lubrication or hydrodynamic rheophysical regimes as summarized by *Coussot and Ancey* [1999].

Pe is the ratio between hydrodynamic forces due to shear and the forces of Brownian motion [*Jomha et al.*, 1991; *Stickel and Powell*, 2005]. It is given by

$$\mathrm{Pe} = \frac{6\pi\eta_l a^3 \dot{\gamma}}{kT}, \tag{4}$$

where k is the Boltzmann constant, a is the particle radius, and T is the absolute temperature. For our experiments, $\mathrm{Pe} \geq 10^3$, indicating negligible Brownian motion. Re_p quantifies the relative importance of inertial and viscous forces at the particle scale [*Stickel and Powell*, 2005], defined as

$$\mathrm{Re}_p = \frac{\rho_l a^2 \dot{\gamma}}{\eta_l}, \tag{5}$$

where ρ_l is the density of the suspending liquid. For all of our experiments, $\mathrm{Re}_p \ll 1$ and inertial forces are negligible. The degree of liquid-solid coupling is indicated by St, defined as the ratio of the characteristic time scale of particle motion as a consequence of viscous drag $\rho_p a^3 / L\eta_l$, to the characteristic time scale of deformation [*Coussot and Ancey*, 1999]. It is given by

Table 3. Suspension Types Used in the Experiments

Suspension	Suspension Types	Total Solid Volume Fration (ϕ)	Volume Fraction of Smaller/Fibrous Particles (ϕ_f)	Schematic Representation	Symbol
Unimodal					
Unimodal	s	0.10, 0.20 0.30, 0.50			
Unimodal	S	0.10, 0.30 0.40, 0.50			
Unimodal	e	0.10, 0.20 0.25, 0.30			
Unimodal	E	0.10, 0.20 0.30, 0.47			
Bimodal $\phi_f = 0.25$					
Bimodal	Ss	0.10, 0.30 0.40, 0.60	0.25		
Bimodal	Se	0.10, 0.20 0.30, 0.40	0.25		
Bimodal	Ee	0.10, 0.20 0.30, 0.35	0.25		
Bimodal	se	0.10, 0.20 0.30, 0.40	0.25		
Bimodal	sE	0.10, 0.20, 0.30 0.40, 0.50	0.25		
Bimodal $\phi = 0.30$					
Bimodal	Ss	0.30	0.50, 0.75		
Bimodal	Se	0.30	0.50, 0.75		
Bimodal	Ee	0.30	0.50, 0.75		
Bimodal	se	0.30	0.50, 0.75		
Bimodal	sE	0.30	0.50, 0.75		

$$\mathrm{St} = \frac{\rho_p a^3 \dot{\gamma}}{L \eta_l}, \tag{6}$$

where ρ_p is the particle density, and L is the characteristic length scale of the particle ($\approx a$) [*Coussot and Ancey*, 1999]. In all experiments, St $\ll$ 1, indicating that the particles are strongly coupled to the suspending liquid under shear.

The ratio of the characteristic settling time for fastest settling particles (the large glass spheres) to the experimental time scale is <1 at $\phi = 0.1$ and $<<1$ at $\phi = 0.5$, following the formulations of *Richardson and Zaki* [1954]. Consequently, the particle settling was negligible during the experiments.

3.5. Shear Experiments

To understand the relationship between shear stress and shear rate, controlled shear stress experiments were performed in parallel-plate geometry (Figure 4d) using an Anton Paar Physica MCR 301^{TM} rotational rheometer. The suspensions were placed between two 25 mm diameter plates at a gap thickness of 1 mm for suspensions "s" and 1.5 mm for all other suspensions. During all experiments, a range of torque was applied on the upper plate, while the resultant angular velocity was recorded. The corresponding applied shear stress, τ, and the resultant shear rate, $\dot{\gamma}$, were calculated from the applied torque, M, and the resultant angular velocity, ω, using $\tau = 2M/\pi r_p^3$ and $\dot{\gamma} = \omega r_p/h$, where h and r_p are the gap thickness and the plate radius, respectively [*Mezger*, 2006].

For each suspension type (Table 3), τ was varied logarithmically from values of 0.01 to 6000 Pa, in order to obtain measurements across a wide range of values [e.g., *Heymann et al.*, 2002]. Experimental results for concentrated suspensions ($\phi/\phi_m > 0.8$) were compared to experimental results with longer ramp time and also with incrementally increasing stress (stress-step intervals), where the maximum difference in apparent

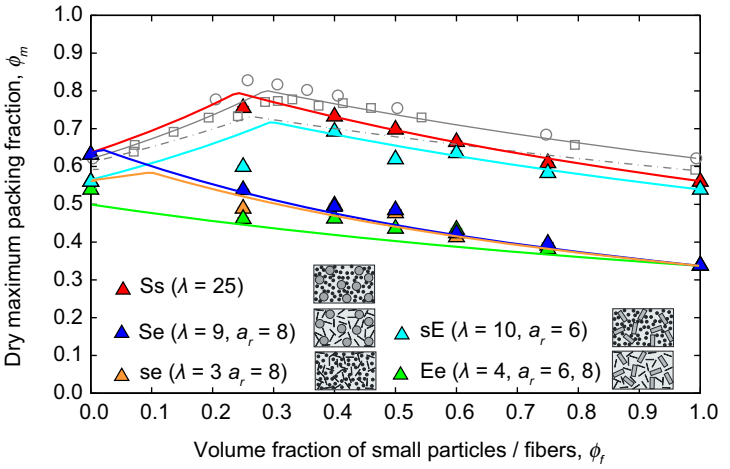

Figure 5. Dry maximum packing fraction of the different particle mixtures. The lines are based on the model (equation (7)) of *Boumonville et al.* [2005], assuming an equivalent spherical diameter for fibers. λ is the ratio of particle diameters, approximated by the equivalent spherical diameter for fibers, whereas a_r is the aspect ratio of elongated particles. Open symbols are the data by *McGeary* [1961] for bimodal spheres and by *Milewski* [1973] for mixture of spheres and fibers. A value of $\phi_f = 0$ corresponds to a unimodal mixture of large or spherical particles ("S" or "s" or "E"), whereas $\phi_f = 1$ represents a unimodal mixture of small or fibrous particles ("s" or "e" or "E"). Error bars are smaller than the symbol size.

suspension viscosity, obtained across the shear rates of interest, is within a factor of 2.5. To eliminate any normal stress associated with sample loading, suspensions of spherical particles with $\phi \geq 0.5$ were subjected to a low strain amplitude oscillation of 1 Hz frequency and 0.01 strain amplitude for 30 s prior to the actual experiment. Suspensions with non-spherical particles were pre-sheared to a strain of up to 100, in order to achieve reproducible measurements [*Jeffery*, 1922; *Marti et al.*, 2005; *Mueller et al.*, 2010].

4. Results

4.1. Dry Maximum Packing Fraction

Following the procedure outlined in section 3.3, the average value of ϕ_m, from 20 repeated measurements, was determined for each particle mixture, with the results shown in Figure 5. For each mixture, the value of ϕ_m depends on the relative fraction of small particles, ϕ_f, in a unique manner that can be predicted using the formulation of *Bournonville et al.* [2005]

$$\phi_m = \min\left[\phi_m^s, \phi_m^l\right], \tag{7}$$

where,

$$\phi_m^s = \frac{\phi_{rcp}^s}{1-(1-\phi_f)\left[1-\phi_{rcp}^s+b_{sl}\left(\phi_{rcp}^s-1\right)\right]}, \tag{8}$$

and

$$\phi_m^l = \frac{\phi_{rcp}^l}{1-\phi_f\left(1-a_{ls}\right)}. \tag{9}$$

Here ϕ_f is the volume fraction of smaller or fibrous particles, whereas ϕ_{rcp}^s and ϕ_{rcp}^l are the packing fractions of unimodal smaller and larger particles, respectively. ϕ_m^s and ϕ_m^l are the maximum packing fractions of smaller and larger unimodal particles, respectively. Furthermore, fitting parameters b_{sl} and a_{ls} are defined as

$$b_{sl} = \left[1-\left(1-\frac{1}{\lambda}\right)^{1.79}\right]^{\beta_1}, \tag{10}$$

and

$$a_{ls} = \left[1-\left(1-\frac{1}{\lambda}\right)^{1.13}\right]^{\beta_2}. \tag{11}$$

Here $\beta_1 = 0.82$ and $\beta_2 = 0.57$ are values obtained by *Bournonville et al.* [2005] for bimodal particle mixtures, whereas for the mixture "se," $\beta_1 = 2$ and $\beta_2 \approx 0.5$, obtained by least squares fitting of the measured values, with the sum of residual squares approximately equal to 0.003. λ is the particle size ratio, defined as ratio of radii of two particles, using the diameter of an equivalent sphere for elongated particles.

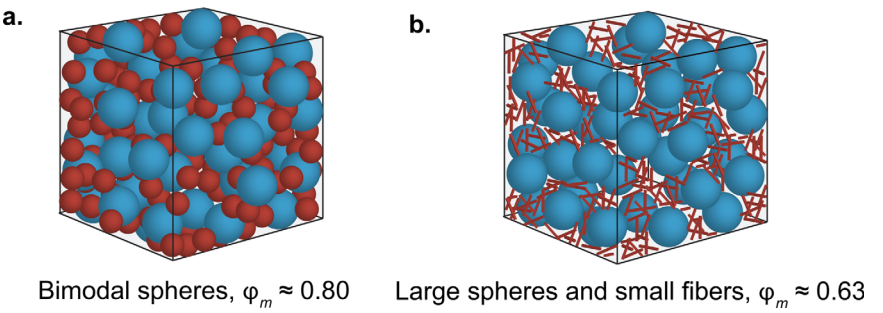

Figure 6. Diagrams illustrating the effect of particle aspect ratio, a_r, and size ratio, λ, on maximum dry packing fraction, ϕ_m. In comparison to the (a) bimodal spherical particles, (b) high aspect ratio particles, due to entanglement and local caging, create more excluded volume (open void space in-between adjacent particles).

For each mixture, the value of ϕ_m has a distinct maximum that depends on ϕ_f, ϕ_{rcp} and λ. For the bimodal spheres, "Ss," the maximum packing was obtained at $\phi_f = 0.25$, whereas for "sE," the maximum packing was obtained at approximately $\phi_f = 0.4$. The other particle mixtures (Se, se, and Ee) have relatively small values of λ, and the maximum packing decreases with increasing volume proportion of elongated particles.

The variation in ϕ_m can be explained by the efficiency of the smaller particles to fit in-between larger particles (Figures 6a and 6b). ϕ_m decreases with increasing particle aspect ratio, a_r, due to the formation of excluded volume [e.g., *Williams and Philipse*, 2003], which is referred to as the volume of space around a particle that is not reachable or can not be occupied by the surrounding particles [e.g., *Philipse*, 1996; *Liu et al*., 2014]. Randomly oriented high aspect ratio particles create local caging of void space in contact with the adjacent particles. Such void space or excluded volume increases with increasing particle aspect ratio, which is the reason for decreasing ϕ_m with increasing particle aspect ratio. Furthermore, with increasing λ interparticle spaces can be occupied by a larger number of small particles, thus also increasing ϕ_m [*Milewski*, 1973]. The difference in maximum packing for the sphere-sphere mixture ("Ss") and for the sphere-fiber mixture ("Se") suggest that the excluded volume, created by the larger particles, can be filled up by low aspect ratio small particles more easily than by high aspect ratio small particles [e.g., *Milewski*, 1973].

4.2. Rheology

4.2.1. Shear Stress and Shear Rate

All suspensions, except those with small ϕ, exhibit a change in $d\tau/d\dot{\gamma}$ with increasing τ (Figure 7). Correspondingly, the apparent suspension viscosity, η_s, first increases and then decreases with increasing $\dot{\gamma}$. The initial increase and resultant peak of η_s are the consequence of a rheological transition from solid to liquid-like response [*Heymann et al*., 2002; *Coussot*, 2007; *Heymann and Nuri*, 2007]. Fitting this part of the data requires specification of an apparent yield stress, τ_y, which is indicative of the existence of the solid to liquid-like rheological transition. With further increase in shear stress, η_s becomes a monotonically decreasing function of $\dot{\gamma}$, with the cause for this shear-thinning a subject of debate [e.g., *Vona et al*., 2011]. The accelerated rate of decrease in viscosity at high shear rates, typically about $\dot{\gamma} > 1-10\text{s}^{-1}$, usually coincided with observable slip between sample and plates. Any data that may be affected by slip are disregarded during subsequent analysis. Overall, η_s increases with ϕ for any given suspension type, as will be discussed in more detail.

For each suspension type, we performed a minimum of two experiments, in order to ascertain reproducibility. The maximum difference in apparent suspension viscosity, at a given shear rate, is within a factor of 5 between two experiments of the same suspension type. Variations in reproducibility are most likely due to small differences in sample preparation and sample placement on the rheometer. These errors are reflected in the spread between minimum and maximum values in the estimated parameters K_r, n, and τ_y for repeat experiments with the same suspension type and are shown as error bars about the average values. The flow curves of τ versus $\dot{\gamma}$ above the rheological transition and below the plate-slip instability were fitted by the Herschel-Bulkley model (equation (3)), using an objective function, F, which is the root-mean-square error between predicted and measured values of τ at the N different values of $\dot{\gamma}$

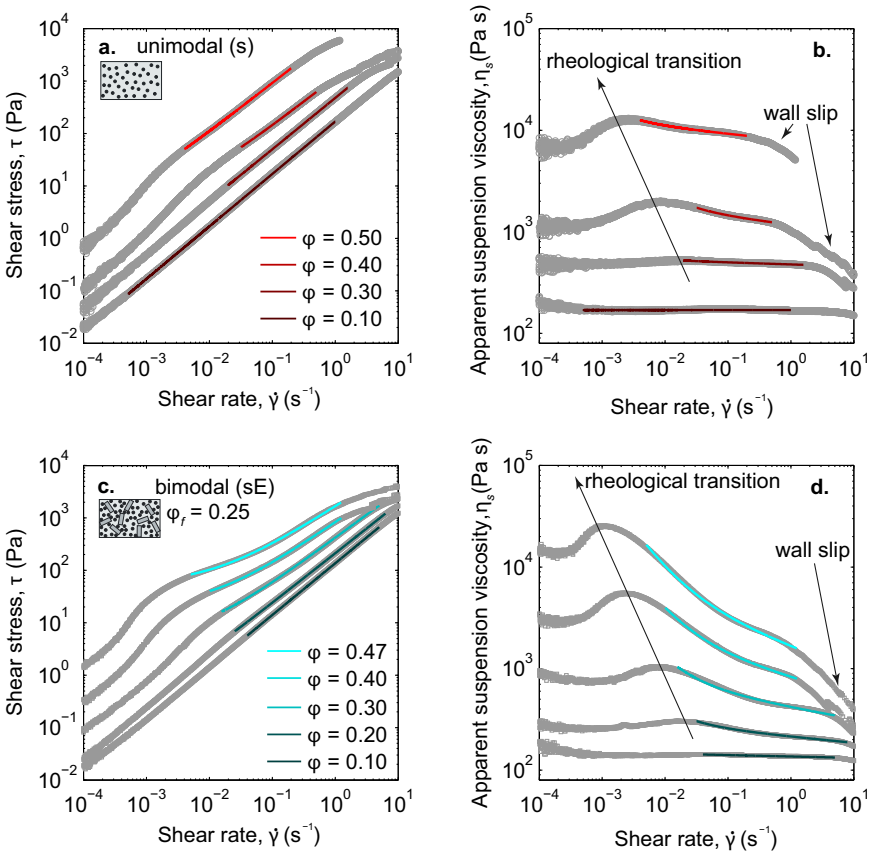

Figure 7. Examples of experimental data (a and b) for unimodal suspension, "s," and (c and d) for bimodal suspension "sE" with $\phi_f = 0.25$, with applied shear stress, τ, as a function of measured shear rate, $\dot{\gamma}$, in Figures 7a and 7c and τ as a function of apparent viscosity, η in Figures 7b and 7d. Superimposed on the data are the best fitting Herschel-Bulkley models (equation (3)) shown over the range of data to which they were fitted. "Rheological transition" refers to the solid-like to liquid-like behavior of suspensions as discussed in section 4.2.1. Accelerated decrease in η_s at higher shear rates are due to the observable slip between sample and plates.

$$F = \sqrt{\frac{1}{N}\sum\left(\frac{\tau_{\text{measured}} - \tau_{\text{predicted}}}{\tau_{\text{measured}}}\right)^2}. \tag{12}$$

Throughout our analysis, $500 \leq N \leq 1100$, and the resultant values of predicted and observed τ are shown in Figure 8 for all experiments.

4.2.2. Consistency, K, at Constant ϕ_f

Consistency, K, is equal to η_s at $n = 1$, whereas the normalized consistency K_r is defined as K/η_l (with a non-integer unit of s^{n-1}). For $\phi_f = 0.25$, we find that K_r always increases with ϕ (Figure 9a), following a Maron-Pierce type model (Table 1) [*Maron and Pierce*, 1956]

$$K_r = \left(1 - \frac{\phi}{\phi_m}\right)^{-\alpha}, \tag{13}$$

where α is a fitting parameter. That ϕ_m is the key parameter controlling K_r is apparent when K_r is plotted as a function of ϕ/ϕ_m (Figure 9b), with K_r tending to infinity as $\phi \rightarrow \phi_m$. At a given ϕ, values of K_r are larger for suspensions with particles of higher aspect ratios, a_r, and/or for smaller particle size ratios, λ (Table 4).

4.2.3. Flow Index, n, at Constant ϕ_f

The flow index determines the dependence of viscosity on shear rate. Our results show a decrease in viscosity with increasing shear rate (i.e., $n < 1$) for all suspension types and at any given ϕ. All else being the same, n decreases with increasing ϕ for a given suspension type. Furthermore, across different suspension types, at a given ϕ, the values of n are smaller for suspensions with particles of larger a_r, and/or with smaller λ (Figure 10a). Some of the existing formulations for n predict values of $n < 0$ at values of $\phi/\phi_m < 1$,

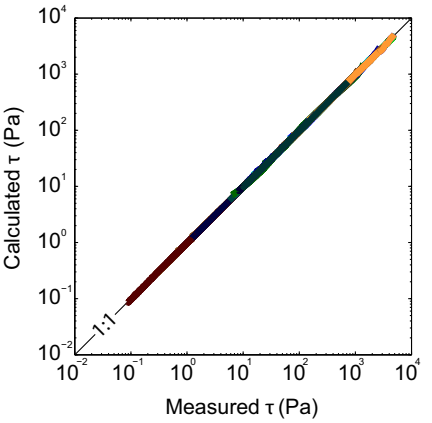

Figure 8. Measured versus calculated shear stress, using the Herschel-Bulkley model (equation (3)), fall within ±0.01 log units for all experiments.

especially in the case of intermediate to high aspect ratio particles [e.g., *Ishibashi*, 2009; *Mueller et al*., 2010]. This is physically unrealistic. Instead, we estimate n as a function of ϕ ($0 \le \phi \le \phi_m$) using

$$n = 1-(1-n_{\min})\left(\frac{\phi}{\phi_{\max}}\right)^{2.3}, \quad (14)$$

where $\phi_{\max}$ is the largest measured value of ϕ for a given mixture type, and $n_{\min}$ is the corresponding value of n at $\phi_{\max}$. Figures 10b–10j show that equation (14) can predict n well for all the suspension types. This functional form of n eliminates the need for unnecessary empirical constants and predicts $n(\phi=\phi_m) > 0$ for all the unimodal and bimodal suspensions. It is also amenable to adjustments in the value of the exponent or in $\phi_{\max}$, should new experimental results necessitate this.

4.2.4. Apparent Yield Stress, τ_y, at Constant ϕ_f

For all suspensions, τ_y increases with increasing ϕ (Figure 11a), becoming of significant value close to the maximum packing ($\phi/\phi_m > 0.8$, Figure 11c), presumably due to particle jamming [e.g., *Liu and Nagel*, 1998; *Song et al*., 2008]. We find that $\tau_y \to 0$ for $\phi/\phi_m \lesssim 0.15$ (Figure 11b) and is consistent with a modified version of the formulation proposed by *Heymann et al*. [2002]

$$\tau_y = \tau^*\left[\left(1-\frac{\phi}{\phi_m}\right)^{-2}-\left(1-\frac{\phi_c}{\phi_m}\right)^{-2}\right]. \quad (15)$$

Here ϕ_c is the critical particle volume fraction below which no significant apparent yield stress could be experimentally determined, and τ^* is a fitting parameter. The values of τ^* tend to be larger for suspensions with higher aspect ratio particles, but we were unable to find a robust predictive relationship for τ^* similar

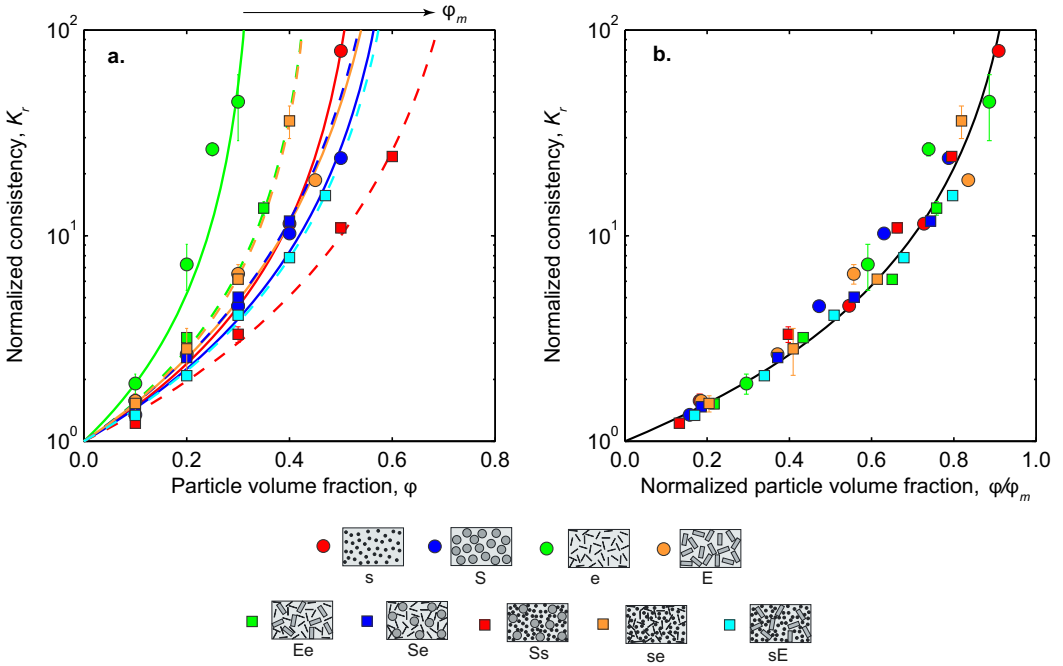

Figure 9. (a) Normalized consistency, K_r (with a noninteger unit of s^{n-1}), as a function of particle volume fraction, ϕ. For each suspension type, denoted by the same symbol and color, the only parameter that changes is ϕ, whereas $\phi_f = 0.25$ remains constant. The corresponding curves show predicted values of K_r using equation (13) with ϕ_m and α in Table 4. (b) K_r as a function of ϕ/ϕ_m, together with the predicted value of $\alpha = 1.92$ for all the data points based on equation (13). Error bars represent the variability in K_r for repeated experiments.

Table 4. Fitting Parameters for Experiments With Unimodal Suspensions and Bimodal Suspensions With $\phi_f = 0.25$, as Used in Equations (13) and (15)

Suspension	ϕ_m	α	τ^*
s	0.56	1.97	0.063
S	0.64	2.16	0.034
e	0.42	3.16	2.776
E	0.34	1.86	0.151
Ss	0.80	2.34	0.335
Se	0.63	1.73	3.742
Ee	0.46	1.80	1.026
se	0.45	2.22	4.402
sE	0.65	2.14	2.644

to some other studies [e.g., *Heymann et al*., 2002; *Mueller et al*., 2010]. Although $\phi_c/\phi_m \approx 0.15$ provides a reasonable match for our experiments, the limited number of experiments at values of $\phi/\phi_m < 0.2$ leaves the potential for further improvements.

4.2.5. Variable ϕ_f

A suite of experiments that fill the entire $\phi - \phi_f$ parameter space are beyond the scope of a single paper. Instead, we have explored two orthogonal subspaces of the $\phi - \phi_f$ parameter space. We tested each of the five different suspension types ("Ss," "Se," "Ee," "se," and "sE") at a constant value of $\phi = 0.30$, but for a range of $0 < \phi_f < 1$. Figures 12 and 13 show for each suspension type the dependence of K_r, n, and τ_y on the particle volume fraction, ϕ, the volume fraction of smaller particles, ϕ_f, and on ϕ/ϕ_m.

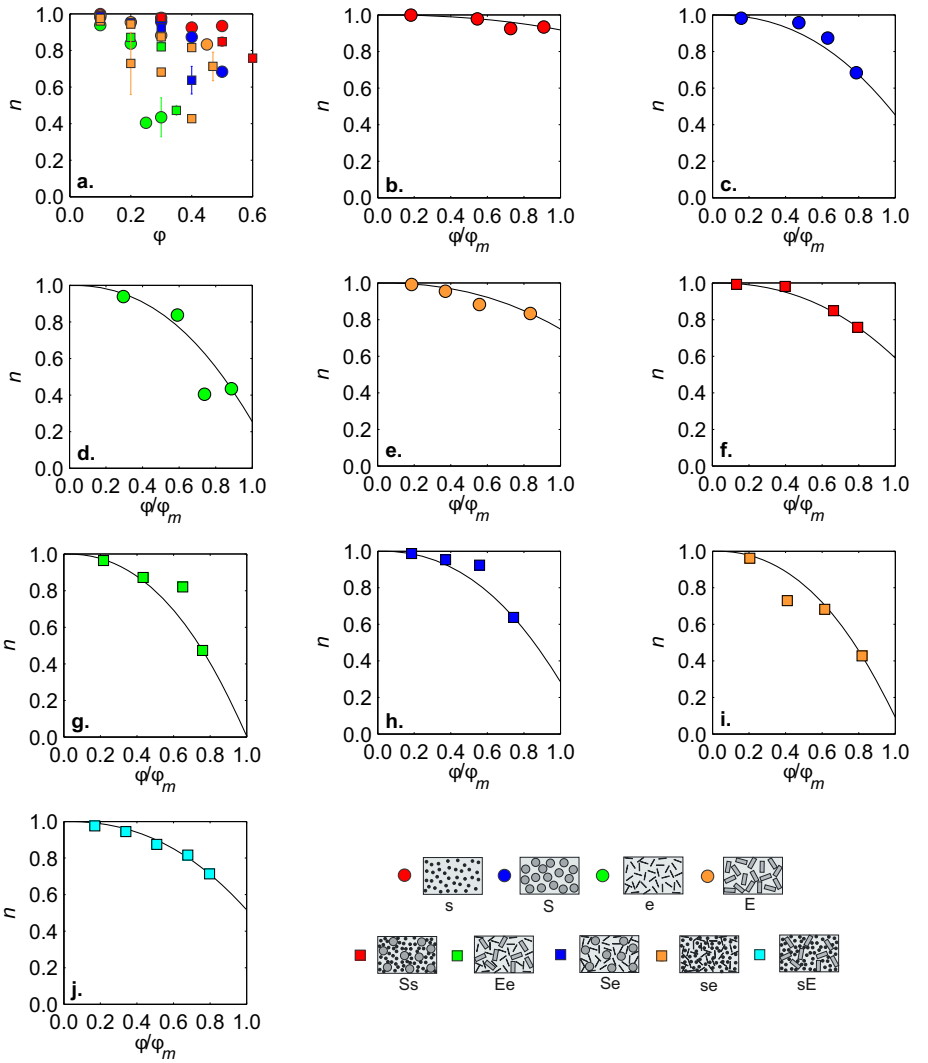

Figure 10. (a) Estimated flow index, n, as a function of particle volume fraction, ϕ, obtained from the Herschel-Bulkley fit (equation (14)) to the experimental data. n decreases with increasing ϕ, and with decreasing particle size ratio, λ. Error bars represent the variability of repeated experiments. (b–j) Model fits to the experimental data of n as function of normalized particle volume fraction, ϕ/ϕ_m, for nine different suspension types using equation (14). Solid curves represent model predictions.

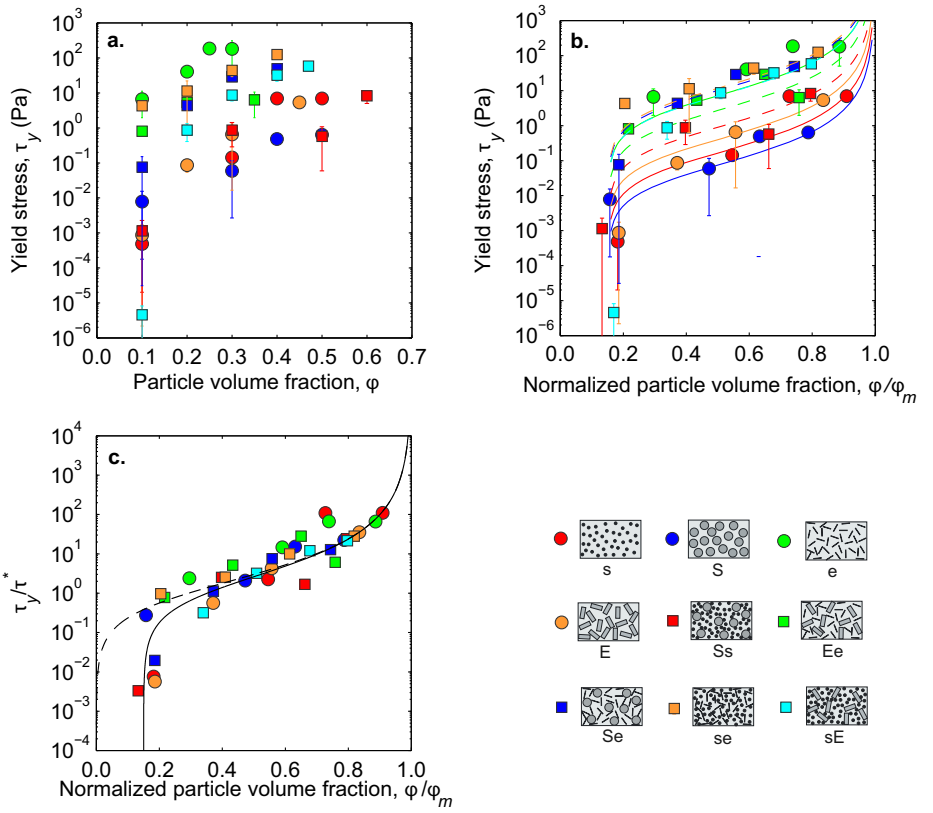

Figure 11. (a) Estimated apparent yield stress, τ_y, as a function of particle volume fraction, ϕ, obtained from the Herschel-Bulkley fit (equation (3)) to the experimental data. Overall, τ_y increases with increasing ϕ and becomes significant as $\phi \rightarrow \phi_m$. (b) τ_y as a function of ϕ/ϕ_m with predictions for individual suspension based on equation (15) are shown as individual curves. (c) Normalized apparent yield stress, τ_y/τ^*, as a function of ϕ/ϕ_m. The black curve is the theoretical prediction based on equation (15), indicating that τ_y vanishes at $\phi_c/\phi_m \approx 0.15$. Predicted estimates of τ_y following *Heymann et al.* [2002] are shown by the dashed gray curve for comparison.

As the reader may recall, for a given suspension type, the maximum packing fraction ϕ_m depends on ϕ_f, as shown in Figure 5, and with a broad trend of decreasing ϕ_m with increasing ϕ_f. The value of K_r strongly depends only on ϕ/ϕ_m (Figure 12) and conforms to equation (13). This is also illustrated in Figure 14a. It is also interesting to point out that K_r can be estimated as a function of ϕ_f using the Farris model (Figure 14b and Table 1) [*Farris*, 1968]. For each suspension type, the value of n also displays a strong dependence on ϕ/ϕ_m (Figure 12), and equation (14) provides an approximate, albeit not perfect, representation. For τ_y, there is considerable scatter about the empirical relation given by equation (15), although in general, τ_y increases with ϕ/ϕ_m.

5. Discussion

5.1. Predictive Quality

The flow behavior of particle-liquid suspensions can be predicted across a wide range of shear rates using the Herschel-Bulkley model, with values of K_r, n, and τ_y that are based on ϕ/ϕ_m, using equations (13)–(15), respectively. The resultant predicted values of τ fall within a factor of two of the measured values (Figure 15). The maximum packing fraction, ϕ_m, has been found to be the key parameter governing the effect of particles on flow behavior, where ϕ_m depends on a_r, λ, and ϕ_f.

The formulations presented herein provide enhanced predictive capabilities that account for the shear-rate dependence of viscosity, which is significant and not directly accounted for in some earlier models of bimodal suspension viscosity [e.g., *Farris*, 1968; *Marti et al.*, 2005; *Cimarelli et al.*, 2011; *Del Gaudio*, 2014]. K_r provides a measure of the effect of particles on viscosity. Equation (13) and Figure 9b indicate that viscosity increases with ϕ/ϕ_m in a predictable manner. The effects of a_r, λ, and ϕ_f are encapsulated by ϕ_m, albeit in a highly nonlinear manner, as conceptually illustrated in Figures 16a and 16b. Physically, viscosity is affected because the particle surface represents a no-slip boundary for the flow of interstitial liquid, and it acts as a

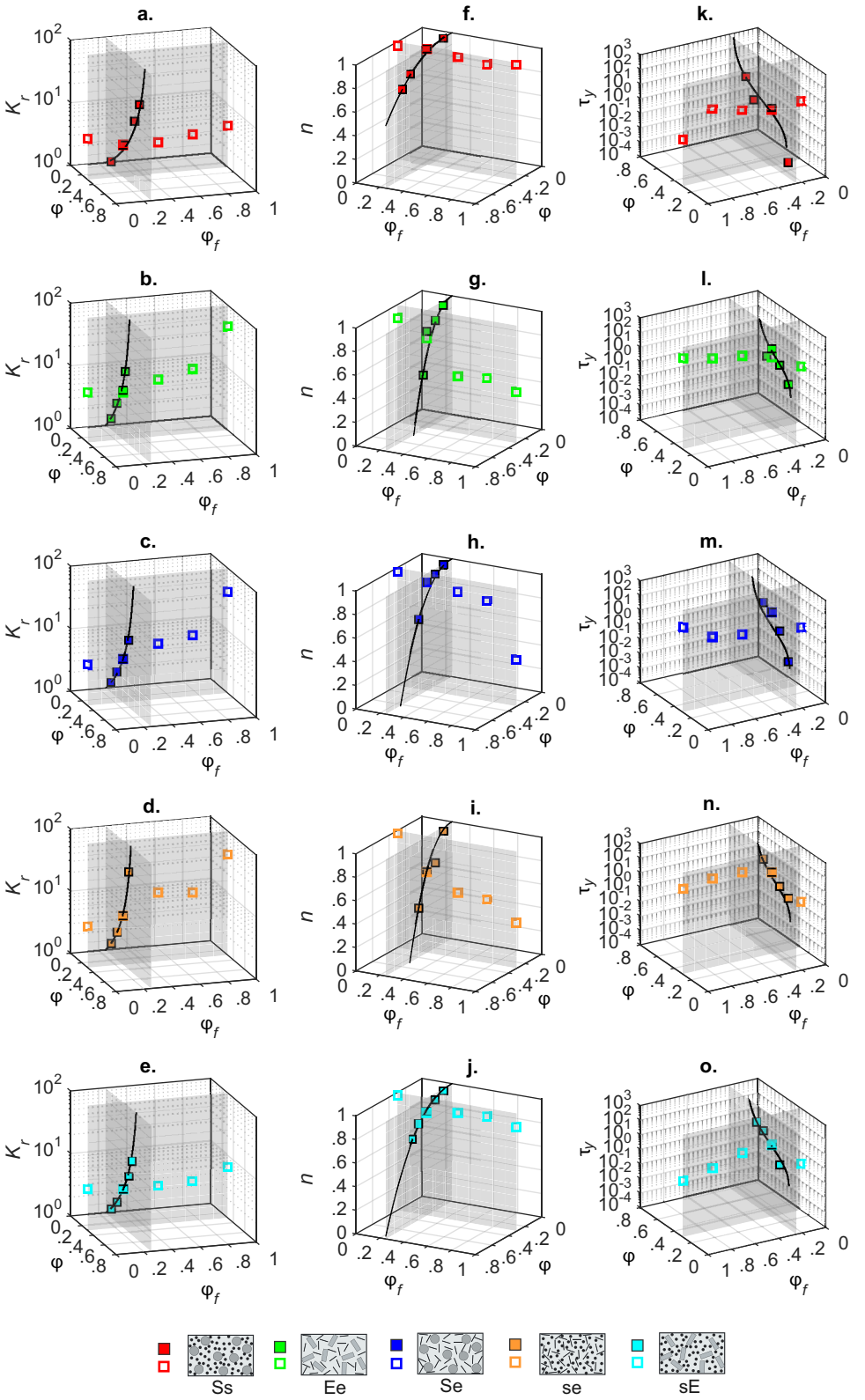

Figure 12. (a–o) Three-dimensional plots showing the functional relationships between the three rheology parameters (normalized consistency, K_r, flow index, n, and yield stress, τ_y), particle volume fraction, ϕ, and volume fraction of finer particles, ϕ_f, for suspension types from both "constant ϕ_f, varying ϕ" (filled squares) and "constant ϕ, varying ϕ_f" (open squares) spaces. Solid lines are based on equations (13)–(15).

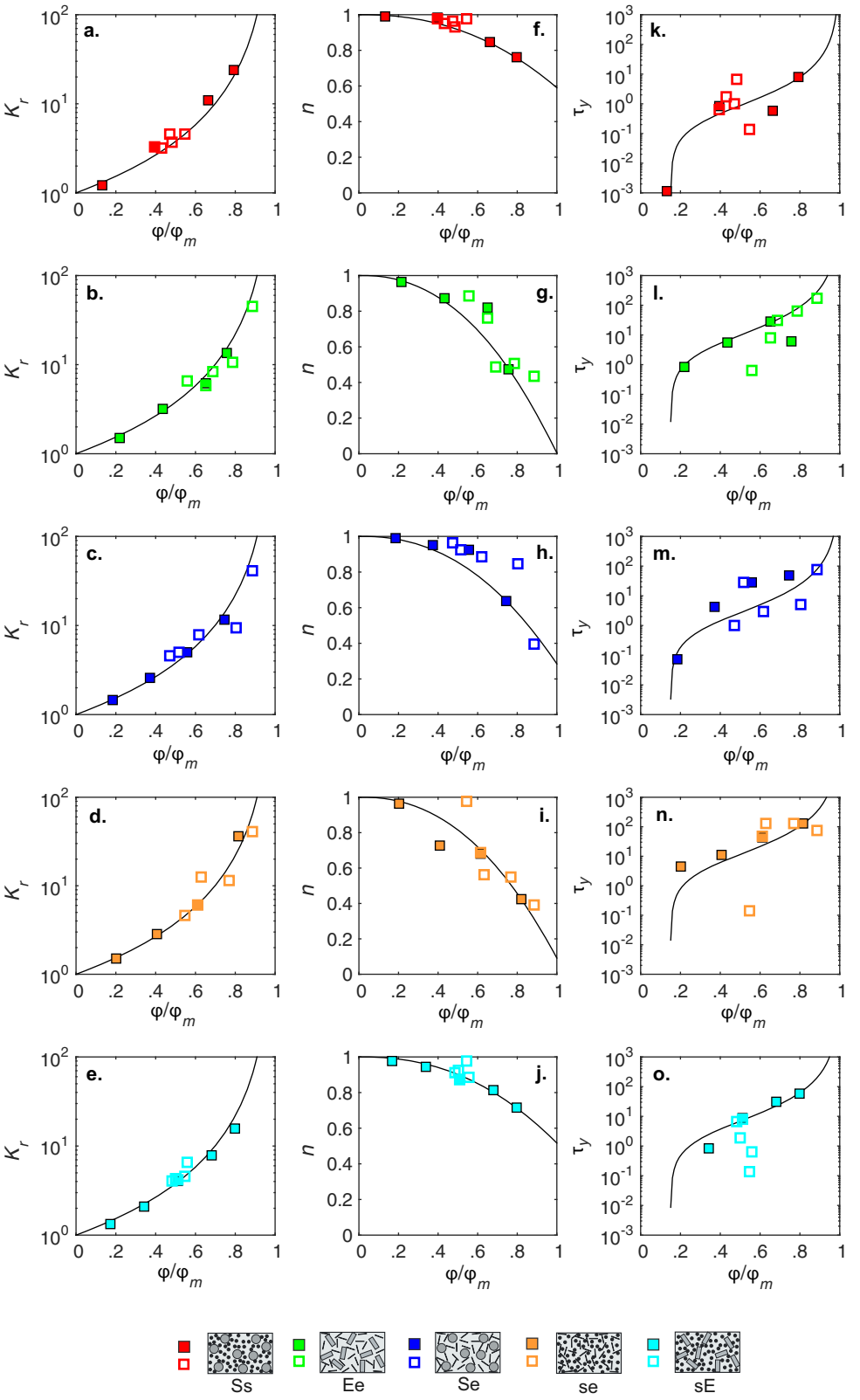

Figure 13. (a–o) Normalized consistency, K_r, flow index, n, and yield stress, τ_y, are shown as function of normalized particle volume fraction, ϕ/ϕ_m, for suspension types from both "constant ϕ_f, varying ϕ" (filled squares) and "constant ϕ, varying ϕ_f" (open squares) spaces. Solid lines are based on equations (13)–(15).

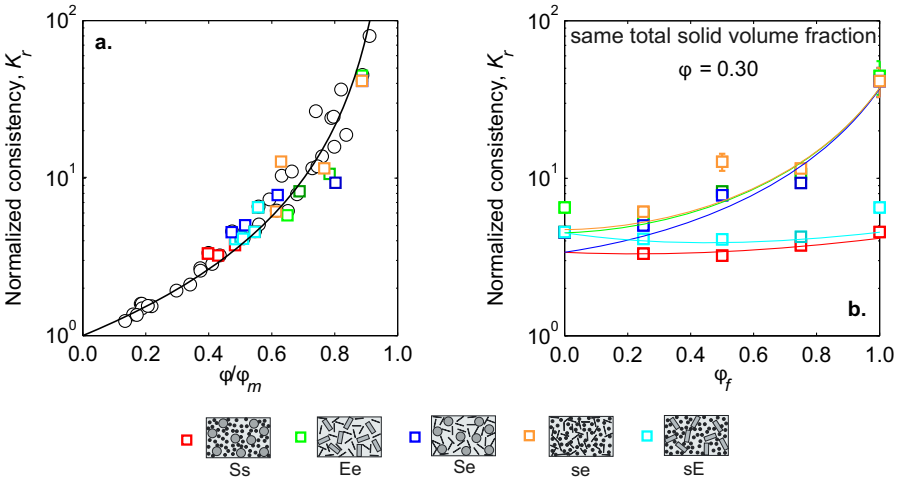

Figure 14. (a) K_r obtained from this $\phi-\phi_f$ space can be well predicted as function of normalized particle volume fraction ϕ/ϕ_m, using equation (13) (open circles represent consistency data from the experiments with "constant ϕ_f, varying ϕ" suspension types). (b) Normalized consistency, K_r versus volume fraction of small particles, ϕ_f. Solid curves are fits of the *Farris* model (Table 1) to K_r.

perturbation to the flow field and steep velocity gradients of the interstitial liquid. Together with the difference in translational motion of individual particles, which leads to particle crowding, this results in increased viscous dissipation. As particles come into closer proximity with one another, this effect becomes more pronounced [*Coussot*, 2005; *Stickel and Powell*, 2005].

5.2. Comparison to Previous Studies

Figure 17 compares our results to previous studies of suspensions with unimodal [*Mueller et al.*, 2010] and bimodal particles [*Castruccio et al.*, 2010; *Cimarelli et al.*, 2011; *Del Gaudio*, 2014], as well as crystalline magmas [*Ishibashi*, 2009; *Vona et al.*, 2011]. K_r can be predicted using equation (13) with all data collapsing onto a single curve (Figure 17a). Variation in the predicted versus measured values (Figure 17b), especially for the data from *Del Gaudio* [2014], may be due to the difference in details of the experimental methods.

Figure 17c shows that the flow index, n, for all experiments can also be reasonably reproduced by equation (14). Figures 17d and 17e show that τ_y estimates from previous experiments approximately correspond to the functional form given by equation (15). However, each suspension type requires a different value of the fitting parameter τ^* (Table 5), perhaps due to the significant sensitivity to the particle aspect ratios and particle size ratio in bimodal particle mixtures, as already highlighted in Figures 12 and 13.

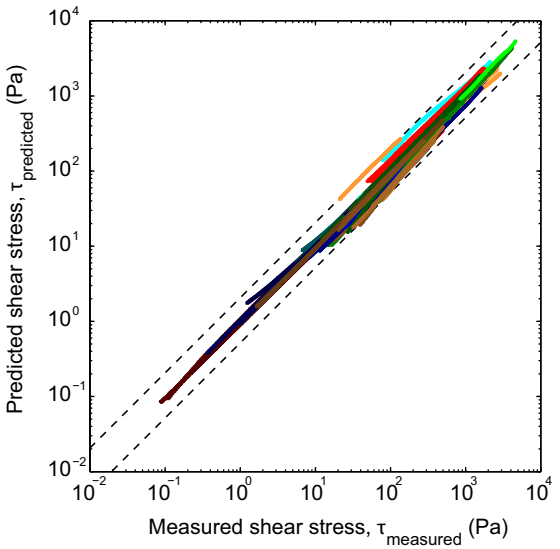

Figure 15. Predicted versus measured shear stress for unimodal suspensions and for bimodal suspensions with ϕ_f=0.25. Predicted values are calculated using equations (3) and (13)–(15). The dashed lines fall within ±0.3 log units of 1:1.

5.2.1. Suspension Viscosity Close to Maximum Packing

A number of studies of concentrated liquid-particle suspensions have been motivated by an interest in unifying suspension and granular rheology [e.g., *Jop et al.*, 2006; *Boyer et al.*, 2011; *Lerner et al.*, 2012; *Maiti and Heussinger*, 2014]. By combining the effect of both frictional and hydrodynamic forces, *Boyer et al.* [2011] proposed

$$\eta_r = 1+\frac{5}{2}\phi(1-\phi/\phi_m)^{-1}+\mu^c(\phi/(\phi_m-\phi))^2, \quad (16)$$

where the friction coefficient μ^c is defined as $\mu^c=\mu_1+(\mu_2-\mu_1)/[1+I_0\phi^2(\phi_m-\phi)^{-2}]$. μ_1 and μ_2

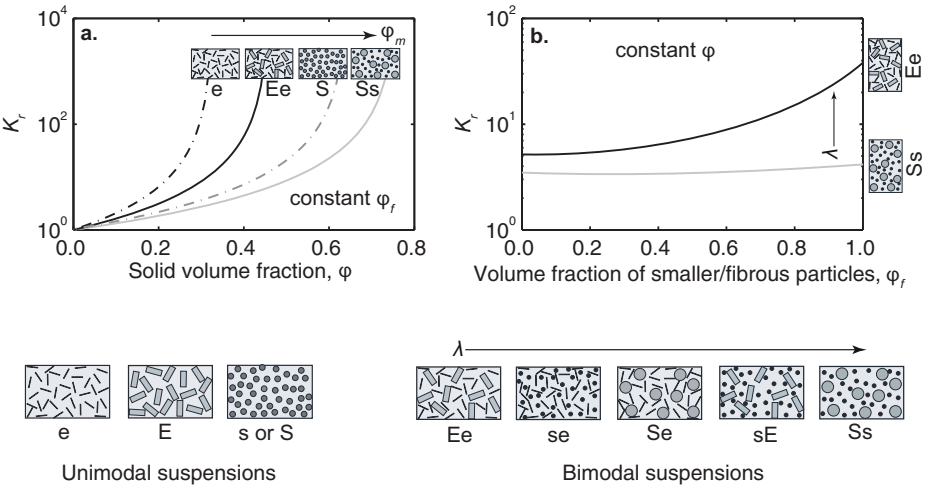

Figure 16. Normalized consistency, K_r, as a function of (a) total solid volume fraction, ϕ, and (b) the volume fraction of smaller/fibrous particles in the suspensions, ϕ_f, following Figures 9a and 14a, respectively. K_r is larger for suspensions with uni to bimodal particles of high aspect ratio, a_r, and for suspensions with bimodal particles of smaller size ratio, λ. As ϕ_m is a function of both a_r and λ, K_r depends on ϕ_m, and tends to infinity as $\phi \rightarrow \phi_m$.

are the minimum and maximum values of friction at zero and high shear rates, respectively, and I_0 is a constant. As $\phi \rightarrow 0$, equation (16) tends to equation (2), applicable for diluted suspension rheology. As $\phi \rightarrow \phi_m$, the effect of particle-particle contact forces become dominant. Comparison of our results for K_r to those of *Boyer et al*. [2011], using equation (16) with $\mu_1 = 0.32$, $\mu_2 = 0.7$ [*Boyer et al*., 2011], and $I_0 = 0.27$ [*Cassar et al*., 2005], indicates remarkable overlap (Figure 18) and robustness of our K_r estimation, even for ϕ/ϕ_m approaching 1.

5.3. Shear Thinning and Effective Viscosity

The dependence of η_r on $\dot{\gamma}$ is significant for $\phi/\phi_m > 0.5$. In our experiments, this led to as much as a 10–100-fold decrease in η_r across 2–3 orders of magnitude change in $\dot{\gamma}$. The physical origin of such shear thinning behavior remains controversial. *Mueller et al*. [2010] attributed it to frictional heating and reduction in the viscosity of the interstitial liquid, whereas, *Ishibashi and Sato* [2007] proposed that the preferred alignment of particles may be the main reason for shear thinning. During our experiments, there was no discernible change in temperature. Change in suspension microstructure may play a dominant role in shear thinning behavior [*Wildemuth and Williams*, 1984; *Vona et al*., 2011], but we cannot offer any substantiating evidence.

An important aspect of equation (13) is the prediction of an infinite viscosity as $\phi \rightarrow \phi_m$ (Figure 9), consistent with the view that at some value of ϕ, particles form interconnected networks that effectively "hinder" the motion of particles past one another, in a process referred to as jamming [*Liu and Nagel*, 1998; *Coussot*, 2005; *Song et al*., 2008]. Because yield stress becomes only significant as $\phi \rightarrow \phi_m$, an effective relative viscosity, η_{eff}, can be defined from the Herschel-Bulkley model with applicability over a wide range of conditions [e.g., *Cimarelli et al*., 2011; *Mueller et al*., 2011]

$$\frac{\eta_s}{\eta_l} \approx \eta_{\text{eff}} = K_r \dot{\gamma}^{n-1}, \tag{17}$$

where K_r and n can be estimated from ϕ/ϕ_m using equations (13) and (14). Figure 19 shows the variation in η_{eff} as a function of $\dot{\gamma}$ and ϕ/ϕ_m. $\eta_{\text{eff}} \rightarrow 1$ as $\phi \rightarrow 0$, however, because of the approximation $\tau_y = 0$, equation (17) is not applicable as $\phi \rightarrow \phi_m$, where τ_y becomes significant. Figure 20a shows that relative viscosity can be predicted to within a factor of two using equation (3). Figure 20b shows the same data, but instead of η_r with η_{eff}, as predicted by equation (17). Although η_{eff} is a reasonable approximation of η_r, the correspondence degrades at low shear rates, that is, close to the rheological transition.

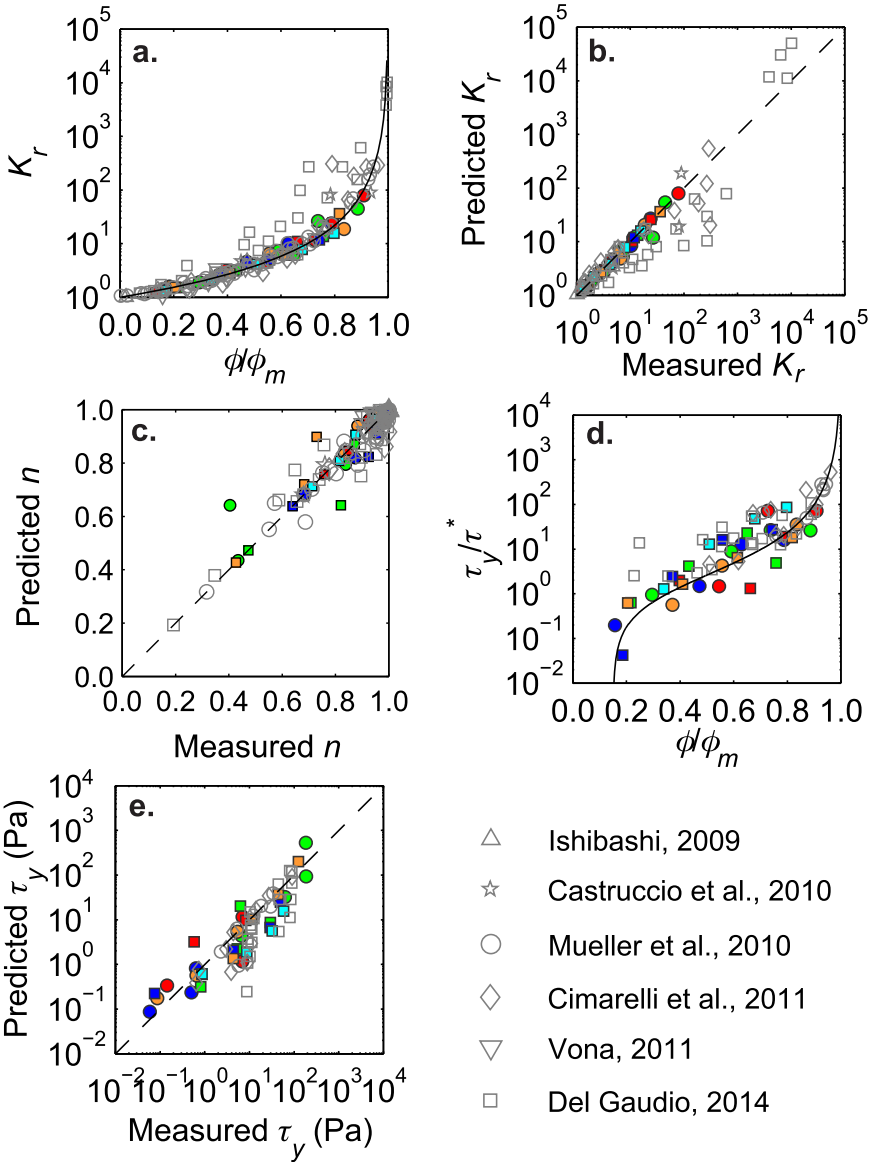

Figure 17. Experimental results from previous studies of suspensions with unimodal [*Mueller et al.*, 2010] and bimodal particles [*Castruccio et al.*, 2010; *Cimarelli et al.*, 2011; *Del Gaudio*, 2014], as well as crystalline magmas [*Ishibashi*, 2009; *Vona et al.*, 2011]. Model fits and quality of predicted values for (a and b) normalized consistency, K_r, (c) flow index, n, and (d and e) yield stress, τ_y are shown based on equations (13)–(15), respectively. Solid lines are predictions using the proposed models in this study, whereas the dashed lines are 1:1 trend to indicate the quality of the predictions.

Table 5. Fitting Parameters ϕ_m *and* τ_y^* (Equations (13) and (15)) for Experimental Results From Previous Studies

Study	Suspension Type	ϕ_m	τ^*
Ishibashi [2009]		0.39	
Castruccio et al. [2010]	50% fine	0.60	
Mueller et al. [2010]	Spherical		
	A		
	B		
	C		
Cimarelli et al. [2011]	AB	0.40	0.139
	CD	0.40	0.051
	AE	0.77	4.36
Vona et al. [2011]			
Del Gaudio [2014]	A	0.50	0.636
	B	0.60	3.599
	0.2Aϕ_B	0.45	1.470
	0.2Bϕ_A	0.45	0.817

6. Implications for Volcanic Eruptions

6.1. Dynamical Similarity

For our experimental results to be applicable to volcanic eruptions, the governing force balances have to be similar, which is the premise of dynamic similarity [e.g., *Kline*, 1986; *Bolster et al.*, 2011]. Here we wish to consider effusive to explosive volcanic eruptions of intermediate to silicic magmas with mass discharge rates of 10^3-10^9 kg s^{-1} [e.g., *Pyle*, 2000], containing crystals of size $10^{-5}\text{m} \lesssim a \lesssim 10^{-2}\text{m}$. Melt viscosities for these compositions are typically $>>$100 Pa s [e.g., *Hui and Zhang*, 2007] and conduit radii are ~10–100 m [e.g., *Jaupart*, 2000]. Furthermore, the difference in density between melt and crystals is on the order of 100 kg m^{-3}. Considering an approximate scaling for shear rate based on the

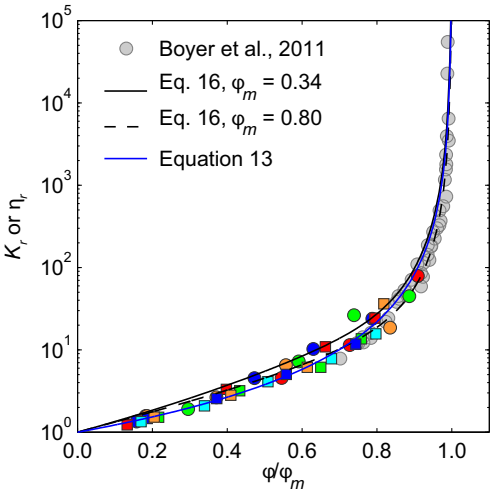

Figure 18. Experimental results of relative consistency from this study (colored symbols) and relative shear viscosity from *Boyer et al.* [2011] as function of normalized particle volume fraction, ϕ/ϕ_m.

average ascent velocity over conduit radius, $\dot{\gamma} \sim 10^{-4}-10^{0}\mathrm{s}^{-1}$. With these approximations, we estimate Pe, Re_p, and St using equations (4)–(6), respectively, and find that St and Re_p are $<<1$, whereas Pe $>> 1$. These values are similar to our analog experiments, which therefore are dynamically similar to magmatic systems across a wide range of conditions (section 3.4, Table 2).

6.2. Conduit Flow of Crystal-Bearing Magma

Here we illustrate how shear-rate-dependent viscosity affects magma flow within volcanic conduits. We assume laminar flow within a cylindrical conduit of radius R, at a volumetric flow rate of Q, and with a Herschel-Bulkley rheology. Because of yield stress, the flow will be comprised of a central plug-like core of radius R_p [*Skelland*, 1967; *Govier and Aziz*, 1982; *Bird et al.*, 1983, 1987; *Chhabra and Richardson*, 2011] with a constant velocity of

$$u_p = \frac{nR}{n+1}\left(\frac{\tau_w}{K}\right)^{1/n}(1-\xi)^{(n+1)/n}. \tag{18}$$

$\tau_w = \Delta PR/2H$ is the wall shear stress, ΔP is the non-hydrostatic pressure difference between the bottom and the top of the conduit, H is the length of the conduit, and $\xi = \tau_y/\tau_w$. The velocity at radii $r > R_p$ is given by

$$u(r) = \frac{nR}{n+1}\left(\frac{\tau_w}{K}\right)^{1/n}\left\{(1-\xi)^{(n+1)/n} - \left(\frac{r}{R}-\xi\right)^{(n+1)/n}\right\}. \tag{19}$$

The volumetric flow rate can be obtained from integrating the velocity across the conduit and is

$$Q = \pi R^3 n(\tau_w/K)^{1/n}(1-\xi)^{(n+1)/n}\left\{\frac{(1-\xi)^2}{3n+1} + \frac{2\xi(1-\xi)}{2n+1} + \frac{\xi^2}{n+1}\right\}. \tag{20}$$

It follows that the average velocity is $u_{\mathrm{avg}} = Q/\pi R^2$.

Figures 21–23 illustrate the effect of τ_y and n on velocity, in particular the strong dependence of apparent viscosity on shear rate. Relatively modest changes in crystal content or size distribution will affect magma

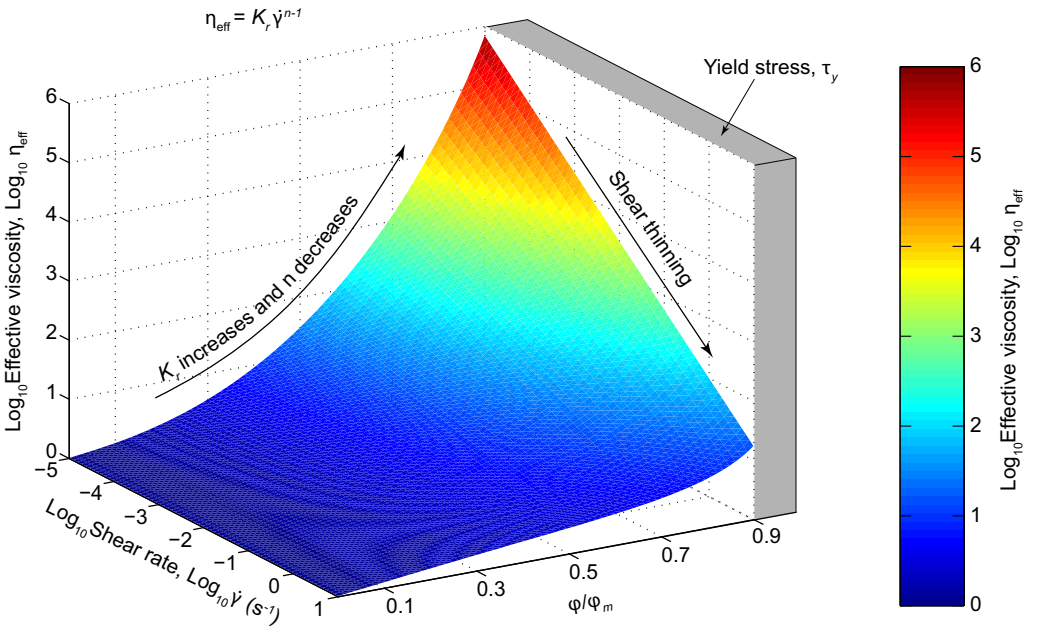

Figure 19. Effective viscosity, η_{eff}, as a function of shear rate, $\dot{\gamma}$, and normalized particle volume fraction, ϕ/ϕ_m, with K_r and n calculated using equations (13) and (14), respectively, for suspension "Se" (Table 4). For $\phi \rightarrow \phi_m$ yield stress, τ_y, is significant and η_{eff} is not valid.

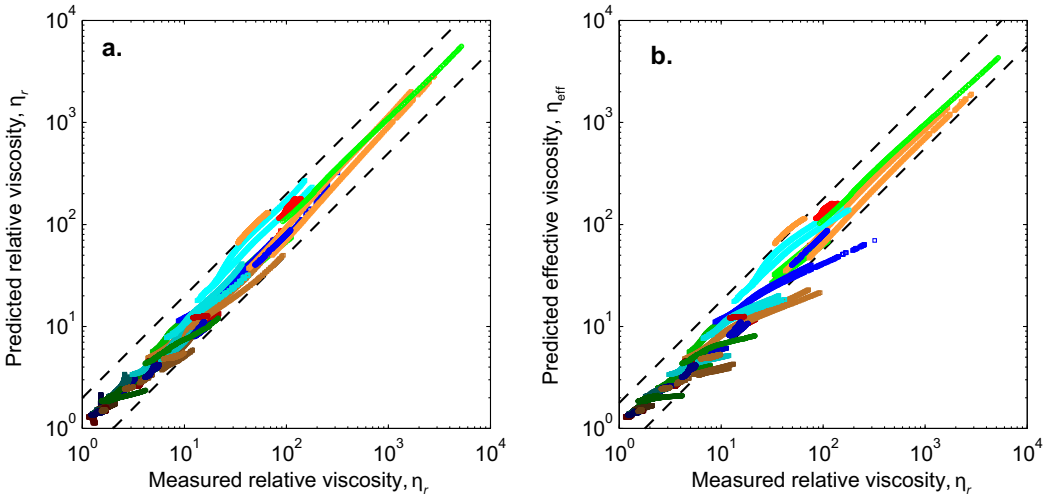

Figure 20. (a) Predicted relative viscosity, η_r, based on equation (3) versus the measured value. All predictions fall within 0.3 log units (dashed lines) of the measured value. (b) Predicted effective viscosity, η_{eff} , based on equation (17) versus measured relative viscosity, η_r. Equation (17) predicts viscosity adequately, except at low values of $\dot{\gamma}$ near the rheological transition, when it results in underpredictions. The graphs show data from experiments with unimodal suspensions and bimodal suspensions with $\phi_f = 0.25$.

discharge rates in a nonlinear fashion, especially at high volume fractions of crystals and for polydisperse crystal size distributions. Furthermore, small changes in the effective pressure gradient may have the potential to affect disproportionally large changes in eruption rate, relative to what would be expected for a Newtonian magma.

Figures 21 and 22 are based on a melt viscosity of $\eta_l = 10^5$ Pa s and a normalized consistency of $K_r = 10$ corresponding to $\phi/\phi_m \approx 0.7$. In Figure 21, the pressure gradient driving flow, $P' = \Delta\rho g \sim 10^4$ Pa m^{-1}, is based on an approximate difference between magmastatic and lithostatic pressure for a density difference between magma and surrounding rock of $\Delta\rho \sim 100$ kg m^{-3}, where g is the acceleration due to gravity. The dimensionless velocity, u/u_{avg}, is shown as function of the dimensionless conduit radius, r/R, for a Newtonian fluid, a Herschel-Bulkley fluid with $n = 0.5$, $\xi = 0$, (yield stress does not affect the flow) and with $n = 0.5$, $\xi = 0.5$ (yield stress significantly affects the flow).

Figure 21a indicates that, while n does affect the shape of the velocity profile, τ_y has the most significant effect that causes the velocity profile to become more plug like. Figure 21b shows the dimensional velocity for the same three cases, illustrating that n has a rather significant effect. Even though K_r is the same for all three cases, it is evident that n can have a tremendous effect on eruption rate during "slow" eruptions, with changes in crystal content potentially affecting large changes in eruption rate. Figure 22a illustrates that all else being the same, the effect of yield stress only becomes significant at very small pressure gradients and $\tau \gtrsim 10^3$ Pa. In

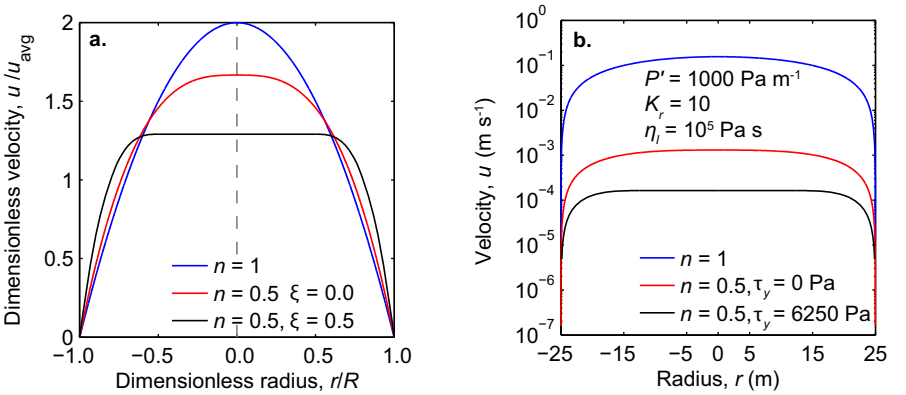

Figure 21. (a) Normalized and (b) dimensional velocity profiles for flow within a conduit. Pressure gradient is 1000 Pa m^{-1} and melt viscosity is 10^5 Pa s.

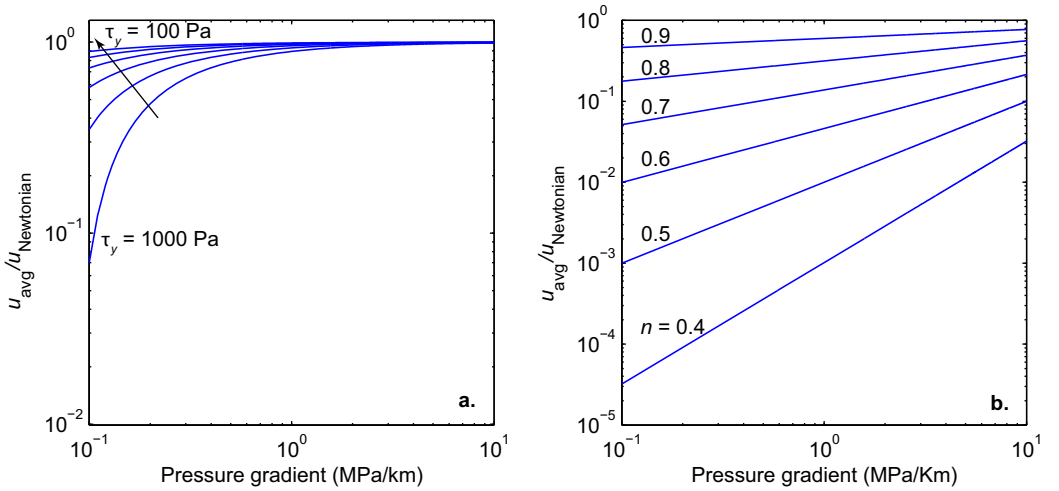

Figure 22. Average velocity of Herschel-Bulkley fluid normalized by the average velocity of a Newtonian fluid as a function of pressure gradient, during flow through a conduit. Conduit radius is 25 m and melt viscosity is 10^5 Pa s. $u_{\text{Newtonian}}/P'$ is approximately 10^{-4} m^2 Pa^{-1} s^{-1}, where P' is the pressure gradient. (a) The effect of τ_y ($n = 1$ and $K_r = 10$) is only significant for small pressure gradients and, hence, low discharge rates. (b) The effect of n ($\tau_y = 0$ and $K_r = 10$) is significant across a wide range of pressure gradients and, hence, discharge rates.

contrast, Figure 22b shows that for non-magmastatic pressure gradients within the likely range of volcanic eruptions ($P' << 100$ MPa km^{-1}), the effect of n is significant, potentially leading to orders of magnitude difference in discharge rate.

Figure 23 illustrates the effect of shear-rate dependence, that is, $n < 1$. A non-magmastatic pressure gradient of 2 MPa km^{-1} is assumed, which would approximately equate to several MPa magma chamber pressure in excess of lithostatic pressure. The conduit is assumed to be cylindrical with a diameter of 30 m [e.g., *Melnik and Sparks*, 1999] and the viscosity of the melt is assumed to be 10^5 Pa s. Two example suspension types are assumed, "Ss" (red) and "Se" (blue), illustrating the potential orders of magnitude difference in resultant average ascent velocity, u_{avg}, all else being equal. Also shown are the corresponding velocities, where shear-thinning has been neglected ($n = 1$), as opposed to the value predicted from a Herschel-Bulkley model for suspensions "Ss" and "Se."

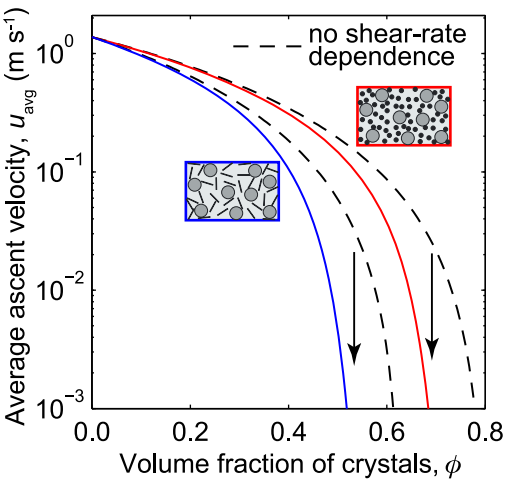

Figure 23. Average ascent velocity, u_{avg} as a function of crystal volume fraction ϕ. Red and blue curves are for the Herschel-Bulkley model for suspensions "Ss" and "Se," respectively, whereas the black dashed curves are the predicted values of u_{avg} for no shear-rate dependence, that is $n = 1$. Note that the neglect of shear-rate dependence can result in large discrepancies of predictions. Assumed driving pressure gradient is 2 MPa km^{-1}, conduit radius is 15 m, and liquid viscosity is 10^5 Pa s.

7. Conclusion

We have investigated the effect of size distribution and shape modality of crystals on magma rheology using analog laboratory experiments that span two orthogonal subspaces of the overall parameter space of crystal volume fraction, size distribution, and shape. Our experiments were fitted by Herschel-Bulkley model. Resultant parameters, consistency, flow index, and apparent yield stress were in turn fitted to empirical formulations that depend on the ratio of volume fraction of particles to their maximum packing fraction. Although a universal model for the dependencies of Herschel-Bulkley parameters on suspension characteristics remains elusive, we have augmented existing predictive capabilities and shown that the Herschel-Bulkley model has promise in this regard. Moreover, our results are fully consistent with new work aimed at unifying suspension and granular rheology.

Our results demonstrate that modest changes in driving pressure, crystal size distribution, or shape modality

have the potential to substantially affect volcanic eruption rates. In particular, one may speculate to what extent small changes in magma chamber pressure, crystal content, and/or size/shape modality may effect magma discharge rates, especially during effusive and dome-forming eruptions. It can, however, be stated with confidence that the shear-rate dependence of viscosity for crystal-rich magmas must be taken into account.

Notation

a	particle radius (m).
a_{ls}	fitting parameter (equation (11)).
a_r	particle aspect ratio.
B	Constant (=2.5, equation(1)).
b_{sl}	fitting parameter (equation (10)).
F	objective function for Herschel-Bulkley (equation (12)).
F_c	compaction force for dry packing tests.
g	gravitation acceleration (m^{-2}).
h	plate-plate gap thickness (m).
H	conduit length (m).
k	Boltzmann constant (1.38×10^{-23} $kgm^2/(s^2\ K)$.
K	consistency (Pa s^n).
K_r	normalized consistency (s^{n-1}).
L	characteristic length scale (m, equation (6)).
L_c	length of sample after compaction (m).
M	torque (N m).
n	flow index.
$n_{\min}$	smallest value of measured n for a suspension.
N	number of experimental data points.
Pe	Peclet number.
P'	pressure gradient (Pa m^{-1}).
Q	volumetric flow rate ($m^3\ s^{-1}$).
r	radial dimension of cylindrical conduit (m).
r_p	parallel plate radius (m).
R	conduit radius (m).
R_p	radius of plug-flow region.
Re	Reynolds number (conduit).
Re_p	particle Reynolds number.
$Re_{crystal}$	Reynolds number of crystalline magma.
St	Stokes number.
T	temperature (°C).
u_{avg}	average velocity (m s^{-1}).
$u_{Newtonian}$	average Newtonian velocity (m s^{-1}).
v_c	volume of large/coarse particles (m^3).
v_f	volume of smaller/fibrous particles (m^3).
v_l	volume of suspending liquid (m^3).
α	fitting parameter (equation (13)).
β_1	fitting parameter (equation (10)).
β_2	fitting parameter (equation (11)).
ΔP	pressure difference (Pa).
η_l	liquid viscosity (Pa s).
η_r	relative viscosity (Pa s).
η_{eff}	effective viscosity $(Pa\ s^{1-n})$ (equation (17)).
η_s	suspension viscosity (Pa s).
γ	strain.
$\dot{\gamma}$	shear rate (s^{-1}).
λ	particle size ratio.

ω	angular velocity (rad s^{-1}).
ϕ	particle volume fraction.
ϕ_c	critical volume fraction for yield stress.
ϕ_m	maximum packing fraction.
$\phi_{\max}$	largest value of measured ϕ for a suspension.
${\phi_m}^s$	maximum packing fraction of smaller particles.
${\phi_m}^l$	maximum packing fraction of coarser/larger particles.
${\phi_{rcp}}^s$	random close packing fraction of unimodal smaller particles.
${\phi_{rcp}}^l$	random close packing fraction of unimodal coarser/larger particles.
ϕ_f	volume fraction of smaller/fibrous particles.
ϕ^c_{Farris}	volume fraction of large particles [*Farris*, 1968].
ϕ^f_{Farris}	volume fraction of small particles [*Farris*, 1968].
ρ	Herschel-Bulkley fluid density.
ρ_l	liquid density (kg m^{-3}).
ρ_p	particle density (kg m^{-3}).
τ	shear stress (Pa).
$\tau_{\text{predicted}}$	predicted shear stress (Pa).
τ_{measured}	measured shear stress (Pa).
τ_w	wall shear stress (Pa).
τ_y	yield stress (Pa).
τ^*	fitting parameter (equation (15)).
ξ	dimensionless yield stress (τ_y/τ_w).

Acknowledgments

We thank Thorsten Becker for editorial handling and George Bergantz, Wim Degruyter, and one anonymous reviewer for their thoughtful and constructive reviews. We also thank Ananya Mallik for helping with the SEM. The raw experimental data plotted in Figure 7 (in gray color) will be available upon request. This material is in part based upon work supported by the National Science Foundation under grants NSF EAR-1019872 and NSF IDR-1015069. Any opinions, findings, and conclusions or recommendations expressed in this material are those of the authors and do not necessarily reflect the views of the National Science Foundation.

References

Bachmann, O., and G. W. Bergantz (2003), Rejuvenation of the Fish Canyon magma body: A window into the evolution of large-volume silicic magma systems, *Geology*, *31*, 789–792, doi:10.1130/G19764.1.

Barnes, H. A. (1999), The yield stress—a review or '$\pi\alpha\nu\tau\alpha\rho\epsilon\iota$'—everything flows?, *J. Non-Newtonian Fluid Mech.*, *81*, 133–178, doi:10.1016/S0377-0257(98)00094-9.

Baule, A., and H. A. Makse (2014), Fundamental challenges in packing problems: From spherical to non-spsherical particles, *Soft Matter*, *10*, 4423–4429.

Bird, R. B., G. C. Dai, and B. J. Yarusso (1983), The rheology and flow of viscoplastic materials, *Rev. Chem. Eng.*, *1*, 1–70.

Bird, R. B., R. C. Armstrong, and O. Hassager (1987), *Dynamics of Polymeric Liquids, Fluid Dynamics*, vol. 1, 2nd ed., pp. 1–672, John Wiley, N. Y.

Bolster, D., R. E. Hershberger, and R. J. Donnelly (2011), Dynamic similarity, the dimensionless science, *Phys. Today*, *64*, 42–47.

Bournonville, B., P. Coussot, and X. Chateau (2005), Modification du modèle de Farris pour la prise en compte desinteractions gèomètriques dun mèlange polydisperse de particules, *Rhèologie*, *7*, 1–8.

Boyer, F., E. Guazzelli, and O. Pouliquen (2011), Unifying suspension and granular rheology, *Phys. Rev. Lett.*, *107*, 188301, doi:10.1103/PhysRevLett.107.188301.

Brouwers, H. J. H. (2006), Particle-size distribution and packing fraction of geometric random packings, *Phys. Rev. E*, *74*, 031309, doi:10.1103/PhysRevE.74.031309.

Caricchi, L., L. Burlini, P. Ulmer, T. Gerya, M. Vasalli, and P. Papale (2007), Non-Newtonian rheology of crystal-bearing magmas and implications for magma ascent dynamics, *Earth Planet. Sci. Lett.*, *264*, 402–419, doi:10.1016/j.epsl.2007.09.032.

Cashman, K. V., and B. D. Marsh (1988), Crystal size distribution (CSD) in rocks and the kinetics and dynamics of crystallization. 2. Makaopuhi lava lake, *Contrib. Mineral. Petrol.*, *99*, 292–305, doi:10.1007/BF00375363.

Cashman, K. V., C. Thornber, and J. P. Kauahikaua (1999), Cooling and crystallization of lava in open channels, and the transition of Pāhoehoe Lava to'A'ā, *Bull. Volcanol.*, *61*, 306–323, doi:10.1007/s004450050299.

Cassar, C., M. Nicolas, and O. Pouliquen (2005), Submarine granular flows down inclined planes, *Phys. Fluid.*, *17*, 103301, doi:10.1063/1.2069864.

Castruccio, A., A. C. Rust, and R. S. J. Sparks (2010), Rheology and flow of crystal-bearing lavas: Insights from analogue gravity currents, *Earth Planet. Sci. Lett.*, *297*, 471–480, doi:10.1016/j.epsl.2010.06.051.

Castruccio, A., A. C. Rust, and R. S. J. Sparks (2014), Assessing lava flow evolution from post-eruption field data using Herschel–Bulkley rheology, *J. Volcanol. Geotherm. Res.*, *275*, 71–84, doi:10.1016/j.jvolgeores.2014.02.004.

Champallier, R., M. Bystricky, and L. Arbaret (2008), Experimental investigation of magma rheology at 300MPa: From pure hydrous melt to 75 vol. % of crystals, *Earth Planet. Sci. Lett.*, *267*, 571–583, doi:10.1016/j.epsl.2007.11.065.

Chang, C., and R. L. Powell (1993), Dynamic simulation of bimodal suspensions of hydrodynamically interacting spherical particles, *J. Fluid. Mech.*, *253*, 173–209.

Chang, C., and R. L. Powell (1994), Effect of particle size distributions on the rheology of concentrated bimodal suspensions, *J. Rheol.*, *38*, 85–98, doi:10.1122/1.550497.

Chevrel, M. O., T. Platz, E. Hauber, D. Baratoux, Y. Lavallée, and D. B. Dingwell (2013), Lava flow rheology: A comparison of morphological and petrological methods, *Earth Planet. Sci. Lett.*, *384*, 109–120, doi:10.1016/j.epsl.2013.09.022.

Chhabra, R. P., and J. F. Richardson (2011), *Non-Newtonian Flow and Applied Rheology: Engineering Applications*, pp. 1–518, Butterworth-Heinemann, Oxford.

Chong, J. S., E. B. Christiansen, and A. D. Baer (1971), Rheology of concentrated suspensions, *J. Appl. Polym. Sci.*, *15*, 2007–2021, doi:10.1002/app.1971.070150818.

Cimarelli, C., A. Costa, S. Mueller, and H. M. Mader (2011), Rheology of magmas with bimodal crystal size and shape distributions: Insights from analog experiments, *Geochem. Geophys. Geosyst.*, *12*, Q07024, doi:10.1029/2011GC003606.
Costa, A., L. Caricchi, and N. Bagdassarov (2009), A model for the rheology of particle-bearing suspensions and partially molten rocks, *Geochem. Geophys. Geosys*. *10*, Q03010, doi:10.1029/2008GC002138.
Coussot, P. (2005), *Rheometry of Pastes, Suspensions, and Granular Materials: Applications in Industry and Environment*, p. 291, John Wiley.
Coussot, P. (2007), Rheophysics of pastes: A review of microscopic modelling approaches, *Soft Matter*, *3*, 528–540, doi:10.1039/B611021P.
Coussot, P., and C. Ancey (1999), Rheophysical classification of concentrated suspensions and granular pastes, *Phys. Rev. E*, *59*, 4445–4457, doi:10.1103/PhysRevE.59.4445.
Cross, M. M. (1970), Kinetic interpretation of non-Newtonian flow, *J. Colloid Interface Sci.*, *33*, 30–35.
Del Gaudio, P., G. Ventura, and J. Taddeucci (2013), The effect of particle size on the rheology of liquid? Solid mixtures with application to lava flows: Results from analogue experiments, *Geochem. Geophys. Geosyst.*, *14*, 2661–2669, doi:10.1002/ggge.20172.
Del Gaudio, P. D. (2014), Rheology of bimodal crystals suspensions: Results from analogue experiments and implications for magma ascent, *Geochem. Geophys. Geosyst.*, *15*, 284–291, doi:10.1002/2013GC005078.
Donev, A., I. Cisse, D. Sachs, E. A. Variano, F. H. Stillinger, R. Connelly, S. Torquato, and P. M. Chaikin (2004), Improving the density of jammed disordered packings using ellipsoids, *Science*, *303*, 990–993, doi:10.1126/science.1093010.
Einstein, A. (1906), Eine neue Bestimmung der Molekl-Dimensionen, *Ann. Phys.*, *19*, 648–661, doi:10.1002/andp.19063240204.
Farris, R. J. (1968), Prediction of the viscosity of multimodal suspensions from unimodal viscosity data, *Trans. Soc. Rheol.*, *12*, 281–301, doi:10.1122/1.549109.
Gay, E. C., P. A. Nelson, and W. P. Armstrong (1969), Flow properties of suspensions with high solids concentrations, *Am. Inst. Chem. Eng. J.*, *15*, 815–822, doi:10.1002/aic.690150606.
Giachetti, T., T. H. Druitt, A. Burgisser, L. Arbaret, and C. Galven (2010), Bubble nucleation, growth and coalescence during the 1997 Vulcanian explosions of Soufrière Hills Volcano, Montserrat, *J. Volcanol. Geotherm. Res.*, *193*, 215–231, doi:10.1016/j.jvolgeores.2010.04.001.
Giordano, D., J. K. Russell, and D. B. Dingwell (2008), Viscosity of magmatic liquids: A model, *Earth Planet. Sci. Lett.*, *271*, 123–134, doi:10.1016/j.epsl.2008.03.038.
Govier, G. W., and K. Aziz (1982), *The Flow of Complex Mixtures in Pipes*, Krieger, Malabar, Fla.
He, D., and N. N. Ekere (2001), Viscosity of concentrated noncolloidal bidisperse suspensions, *Rheol. Acta*, *40*, 591–598, doi:10.1007/s003970100187.
Herschel, W. H., and R. Bulkley (1926), Konsistezmessungen von gummi benzol loesungen, *Colloid Polym. Sci.*, *39*, 291–300, doi:10.1007/BF01432034.
Heymann, L., and A. Nuri (2007), Transition pathways between solid and liquid state in suspensions, *Phys. Rev. E*, *75*, 021505, doi:10.1103/PhysRevE.75.021505.
Heymann, L., S. Peukert, and N. Aksel (2002), On the solid-liquid transition of concentrated suspensions in transient shear flow, *Rheol. Acta*, *41*, 307–315, doi:10.1007/s00397-002-0227-1.
Higgins, M. (1996), Magma dynamics beneath the Kameni volcano, Greece, as revealed by crystal size and shape measurements, *J. Volcanol. Geotherm. Res.*, *70*, 37–48, doi:10.1016/0377-0273(95)00045-3.
Higgins, M. D. (2000), Measurement of crystal size distributions, *Am. Mineral.*, *85*, 1105–1116.
Higgins, M. D. (2006), Verification of ideal semi-logarithmic, lognormal or fractal crystal size distributions from 2D datasets, *J. Volcanol. Geotherm. Res.*, *154*, 8–16, doi:10.1016/j.jvolgeores.2005.09.015.
Higgins, M. D., and J. Roberge (2003), Crystal size distribution of plagioclase and amphibole from Soufrière Hills Volcano, Montserrat: Evidence for dynamic crystallization–textural coarsening cycles, *J. Petrol.*, *44*, 1401–1411, doi:10.1093/petrology/44.8.1401.
Hodge, K. F., G. Carazzo, and A. M. Jellinek (2012), Experimental constraints on the deformation and breakup of injected magma, *Earth Planet. Sci. Lett.*, *325*, 52–62, doi:10.1016/j.epsl.2012.01.031.
Hoover, S., K. V. Cashman, and M. Manga (2001), The yield strength of subliquidus basalts: Experimental results, *J. Volcanol. Geotherm. Res.*, *107*, 1–18, doi:10.1016/S0377-0273(00)00317-6.
Huber, C., O. Bachmann, and J. Dufek (2012), Crystal-poor versus crystal-rich ignimbrites: A competition between stirring and reactivation, *Geology*, *40*, 115–118, doi:10.1130/G32425.1.
Hui, H., and Y. Zhang (2007), Toward a general viscosity equation for natural anhydrous and hydrous silicate melts, *Geochim. Cosmochim. Acta*, *71*, 403–416.
Ishibashi, H. (2009), Non-Newtonian behavior of plagioclase-bearing basaltic magma: Subliquidus viscosity measurement of the 1707 basalt of Fuji volcano, Japan, *J. Volcanol. Geotherm. Res.*, *181*, 78–88, doi:10.1016/j.jvolgeores.2009.01.004.
Ishibashi, H., and H. Sato (2007), Viscosity measurements of subliquidus magmas: Alkali olivine basalt from the Higashi-Matsuura district, Southwest Japan, *J. Volcanol. Geotherm. Res.*, *160*, 223–238, doi:10.1016/j.jvolgeores.2006.10.001.
Jaupart, C. (2000), Magma ascent at shallow levels, in *Encyclopedia of Volcanoes*, vol. 1, pp. 237–245, Academic Press, San Diego, Calif.
Jeffery, G. B. (1922), The motion of ellipsoidal particles immersed in a viscous fluid, *Proc. R. Soc. London, Ser. A*, *102*, 161–179, doi:10.1098/rspa.1922.0078.
Jerram, D. A., and V. M. Martin (2008), Understanding crystal populations and their significance through the magma plumbing system, *Geol. Soc. Spec. Publ.*, *304*, 133–148, doi:10.1144/SP304.7.
Jomha, A. I., A. Merrington, L. V. Woodcock, H. A. Barnes, and A. Lips (1991), Recent developments in dense suspension rheology, *Powder Technol.*, *65*, 343–370.
Jop, P., Y. Forterre, and O. Pouliquen (2006), A constitutive law for dense granular flows, *Nature*, *441*, 727–730, doi:10.1038/nature04801.
Karlstrom, L., J. Dufek, and M. Manga (2010), Magma chamber stability in arc and continental crust, *J. Volcanol. Geotherm. Res.*, *190*, 249–270, doi:10.1016/j.jvolgeores.2009.10.003.
Kerr, R. C., and J. R. Lister (1991), The effects of shape on crystal settling and on the rheology of magmas, *J. Geol.*, 457–467.
Kline, S. J. (1986), *Similitude and Approximation Theory*, 248 pp., Springer, N. Y.
Krieger, I. M. (1972), Rheology of monodisperse latices, *Adv. Colloid Interface Sci.*, *3*, 111–136.
Krieger, I. M., and T. J. Dougherty (1959), A mechanism for non-Newtonian flow in suspensions of rigid spheres, *Trans. Soc. Rheol.*, *3*, 137–152, doi:10.1122/1.548848.
Lavallèe, Y., K. U. Hess, B. Cordonnier, and D. B. Dingwell (2007), Non-Newtonian rheological law for highly crystalline dome lavas, *Geology*, *35*, 843–846, doi:10.1130/G23594A.1.
Lejeune, A. M., and P. Richet (1995), Rheology of crystal-bearing silicate melts: An experimental study at high viscosities, *J. Geophys. Res.*, *100*, 4215–4229, doi:10.1029/94JB02985.
Lerner, E., G. Dring, and M. Wyart (2012), A unified framework for non-Brownian suspension flows and soft amorphous solids, *Proc. Natl. Acad. Sci. U. S. A.*, *109*, 4798–4803, doi:10.1073/pnas.1120215109.
Liu, A. J., and S. R. Nagel (1998), Nonlinear dynamics: Jamming is not just cool any more, *Nature*, *396*, 21–22, doi:10.1038/23819.

Liu, L., P. Lu, L. Meng, W. Jin, and S. Li (2014), Excluded volumes of clusters in tetrahedral particle packing, *Phys. Lett. A*, *378*, 835–838, doi:10.1016/j.physleta.2014.01.023.
Llewellin, E. W., and M. Manga (2005), Bubble suspension rheology and implications for conduit flow, *J. Volcanol. Geotherm. Res.*, *143*, 205–217, doi:10.1016/j.jvolgeores.2004.09.018.
Mader, H. M., M. Manga, and T. Koyaguchi (2004), The role of laboratory experiments in volcanology, *J. Volcanol. Geotherm. Res.*, *129*, 1–5, doi:10.1016/S0377-0273(03)00228-2.
Mader, H. M., E. W. Llewellin, and S. P. Mueller (2013), The rheology of two phase magmas: A review and analysis, *J. Volcanol. Geotherm. Res.*, *257*, 135–158, doi:10.1016/j.jvolgeores.2013.02.014.
Maiti, M., and C. Heussinger (2014), Rheology near jamming: The influence of lubrication forces, *Phys. Rev. E*, *89*, 052308, doi:10.1103/PhysRevE.89.052308.
Manga, M., J. Castro, K. V. Cashman, and M. Loewenberg (1998), Rheology of bubble-bearing magmas, *J. Volcanol. Geotherm. Res.*, *87*, 15–28, doi:10.1016/S0377-0273(98)00091-2.
Maron, S. H., and P. E. Pierce (1956), Application of Ree-Eyring generalized flow theory to suspensions of spherical particles, *J. Colloid Sci.*, *11*, 80–95, doi:10.1016/0095-8522(56)90023-X.
Marsh, B. D. (1988), Crystal size distribution (CSD) in rocks and the kinetics and dynamics of crystallization I. Theory, *Contrib. Mineral. Petrol.*, *99*, 277–291, doi:10.1007/BF00375362.
Marsh, B. D. (1998), On the interpretation of crystal size distributions in magmatic systems, *J. Petrol.*, *39*, 553–599, doi:10.1093/petroj/39.4.553.
Marti, I., O. Hfler, P. Fischer, and E. J. Windhab (2005), Rheology of concentrated suspensions containing mixtures of spheres and fibres, *Rheol. Acta*, *44*, 502–512, doi:10.1007/s00397-005-0432-9.
McBirney, A. R., and T. Murase (1984), Rheological properties of magma, *Annu. Rev. Earth Planet. Sci.*, *12*, 337–357, doi:10.1146/annurev.ea.12.050184.002005.
McGeary, R. K. (1961), Mechanical packing of spherical particles, *J. Am. Ceram. Soc.*, *44*, 513–522, doi:10.1111/j.1151-2916.1961.tb13716.x.
Melnik, O., and R. S. J. Sparks (1999), Nonlinear dynamics of lava dome extrusion, *Nature*, *402*, 37–41, doi:10.1038/46950.
Melnik, O., and R. S. J. Sparks (2002), Dynamics of magma ascent and lava extrusion at Soufrière Hills Volcano, Montserrat, *Geol. Soc. London Memo.*, *21*, 153–171, doi:10.1144/GSL.MEM.2002.021.01.07.
Mezger, T. G. (2006), *The Rheology Handbook: For Users of Rotational and Oscillatory Rheometers*, Vincentz Network GmbH & Co KG, Hannover.
Milewski, J. V. (1973), A study of the packing of milled fibreglass and glass beads, *Composites*, *4*, 258–265, doi:10.1016/0010-4361(73)90392-3.
Moitra, P., H. M. Gonnermann, B. F. Houghton, and T. Giachetti, (2013), Relating vesicle shapes in pyroclasts to eruption styles, *Bull. Volcanol.*, *75*, 1–14, doi:10.1007/s00445-013-0691-8.
Mueller, S., E. W. Llewellin, and H. M. Mader (2010), The rheology of suspensions of solid particles, *Philos. Trans. R. Soc. A*, *466*, 1201–1228, doi:10.1098/rspa.2009.0445.
Mueller, S., E. W. Llewellin, and H. M. Mader (2011), The effect of particle shape on suspension viscosity and implications for magmatic flows, *Geophys. Res. Lett.*, *38*, L13316, doi:10.1029/2011GL047167.
Nguyen, Q. D., and D. V. Boger (1992), Measuring the flow properties of yield stress fluids, *Annu. Rev. Fluid Mech.*, *24*, 47–88, doi:10.1146/annurev.fl.24.010192.000403.
Ouchiyama, N., and T. Tanaka (1981), Porosity of a mass of solid particles having a range of sizes, *Ind. Eng. Chem. Fundam.*, *20*, 66–71, doi:10.1021/i100001a013.
Petford, N. (2009), Which effective viscosity?, *Mineral. Mag.*, *73*, 167–191, doi:10.1180/minmag.2009.
Philipse, A. P. (1996), The random contact equation and its implications for (colloidal) rods in packings, suspensions, and anisotropic powders, *Langmuir*, *12*, 1127–1133, doi:10.1021/la950671o.
Picard, D., L. Arbaret, M. Pichavant, R. Champallier, and P. Launeau (2013), The rheological transition in plagioclase bearing magmas, *J. Geophys. Res.*, *118*, 1363–1377, doi:10.1002/jgrb.50091.
Pinkerton, H., and R. J. Stevenson (1992), Methods of determining the theological properties of lavas from their physicochemical properties, *J. Volcanol. Geotherm. Res.*, *53*, 47–66, doi:10.1016/0377-0273(92)90073-M.
Pistone, M., L. Caricchi, P. Ulmer, L. Burlini, P. Ardia, E. Reusser, F. Marone, and L. Arbaret (2012), Deformation experiments of bubble- and crystal-bearing magmas: Rheological and microstructural analysis, *J. Geophys. Res.*, *117*, B05208, doi:10.1029/2011JB008986.
Prior, J., I. Almeida, and J. M. Loureiro (2013), Prediction of the packing porosity of mixtures of spherical and non-spherical particles with a geometric model, *Powder Technol.*, *249*, 482–496, doi:10.1016/j.powtec.2013.09.006.
Probstein, R. F., M. Z. Sengun, and T. C. Tseng (1994), Bimodal model of concentrated suspension viscosity for distributed particle sizes, *J. Rheol.*, *38*, 811, doi:10.1122/1.550594.
Pyle, D. M. (2000), Sizes of volcanic eruptions, in *Encyclopedia of Volcanoes*, vol. 1, pp. 263–269, Academic Press, San Diego, Calif.
Qi, F., and R. I. Tanner (2011), Relative viscosity of bimodal suspensions, *Korea-Aust. Rheol. J.*, *23*, 105–111, doi:10.1007/s13367-011-0013-7.
Richardson, J. F., and W. N. Zaki (1954), The sedimentation of a suspension of uniform spheres under conditions of viscous flow, *Chem. Eng. Sci.*, *3*, 65–73, doi:10.1016/0009-2509(54)85015-9.
Rust, A. C., M. Manga, and K. V. Cashman (2003), Determining flow type, shear rate and shear stress in magmas from bubble shapes and orientations, *J. Volcanol. Geotherm. Res.*, *122*, 111–132, doi:10.1016/j.jvolgeores.2004.09.018.
Rutgers, Ir. R. (1962), Relative viscosity of suspensions of rigid spheres in Newtonian liquids, *Rheol. Acta*, *2*, 202–210, doi:10.1007/BF01983952.
Ryerson, F. J., H. C. Weed, and A. J. Piwinskii (1988), Rheology of subliquidus magmas, I. Picritic compositions, *J. Geophys. Res.*, *93*, 3421–3436, doi:10.1029/JB093iB04p03421.
Saar, M. O., M. Manga, K. V. Cashman, and S. Fremouw (2001), Numerical models of the onset of yield strength in crystal-melt suspensions, *Earth Planet. Sci. Lett.*, *187*, 367–379, doi:10.1016/S0012-821X(01)00289-8.
Shapiro, A. P., and R. F. Probstein (1992), Random packings of spheres and fluidity limits of monodisperse and bidisperse suspensions, *Phys. Rev. Lett.*, *68*, 1422–1425, doi:10.1103/PhysRevLett.68.1422.
Skelland, A. H. P. (1967), *Non-Newtonian Flow and Heat Transfer*, pp. 82–103, John Wiley, N. Y.
Song, C., W. Ping, and A. M. Hernn (2008), A phase diagram for jammed matter, *Nature*, *453*, 629–632, doi:10.1038/nature06981.
Sparks, R. S. J. (2003), Forecasting volcanic eruptions, *Earth Planet. Sci. Lett.*, *210*, 1–15, doi:10.1016/S0012-821X(03)00124-9.
Sparks, R. S. J., et al. (1998), Magma production and growth of the lava dome of the Soufrière Hills Volcano, Montserrat, West Indies: November 1995 to December 1997, *Geophys. Res. Lett.*, *25*, 3421–3424.
Stickel, J. J., and R. L. Powell (2005), Fluid mechanics and rheology of dense suspensions, *Annu. Rev. Fluid Mech.*, *37*, 129–149, doi:10.1146/annurev.fluid.36.050802.122132.
Sudduth, R. D. (1993), A new method to predict the maximum packing fraction and the viscosity of solutions with a size distribution of suspended particles II, *J. Appl. Polym. Sci.*, *48*, 37–55, doi:10.1002/app.1993.070480105.

Sumita, I., and M. Manga (2008), Suspension rheology under oscillatory shear and its geophysical implications, *Earth. Planet. Sci. Lett.*, *269*, 468–477, doi:10.1016/j.epsl.2008.02.043.

Thomas, D. G. (1965), Transport characteristics of suspension: 8. A note on the viscosity of Newtonian suspensions of uniform spherical particles, *J. Colloid Sci.*, *20*, 267–277, doi:10.1016/0095-8522(65)90016-4.

Torquato, S., T. M. Truskett, and P. G. Debenedetti (2000), Is random close packing of spheres well defined?, *Phys. Rev. Lett.*, *84*, 2064–2067, doi:10.1103/PhysRevLett.84.2064.

Vona, A., C. Romano, D. B. Dingwell, and D. Giordano (2011), The rheology of crystal bearing basaltic magmas from Stromboli and Etna, *Geochim. Cosmochim. Acta*, *75*, 3214–3236, doi:10.1016/j.gca.2011.03.031.

Webb, S. L., and D. B. Dingwell (1990), Non-Newtonian rheology of igneous melts at high stresses and strain rates: Experimental results for rhyolite, andesite, basalt, and nephelinite, *J. Geophys. Res.*, *95*, 15,695–15,701, doi:10.1029/JB095iB10p15695.

Weitz, D. A. (2004), Packing in the spheres, *Science*, *303*, 968–969, doi:10.1126/science.1094581.

Wildemuth, C. R., and M. C. Williams (1984), Viscosity of suspensions modeled with a shear-dependent maximum packing fraction, *Rheol. Acta*, *23*, 627–635, doi:10.1007/BF01438803.

Wildemuth, C. R., and M. C. Williams (1985), A new interpretation of viscosity and yield stress in dense slurries: Coal and other irregular particles, *Rheol. Acta*, *24*, 75–91, doi:10.1007/BF01329266.

Williams, S. R., and A. P. Philipse (2003), Random packings of spheres and spherocylinders simulated by mechanical contraction, *Phys. Rev. E*, *67*, 051301, doi:10.1103/PhysRevE.67.051301.

Yu, A. B., R. P. Zou, and N. Standish (1996), Modifying the linear packing model for predicting the porosity of non-spherical particle mixtures, *Ind. Eng. Chem. Res.*, *35*, 3730–3741, doi:10.1021/ie950616a.

Zhang, Y., Z. Xu, M. Zhu, and H. Wang (2007), Silicate melt properties and volcanic eruptions, *Rev. Geophys.*, *45*, RG4004, doi:10.1029/2006RG000216.

Zhou, J. Z. Q., T. Fang, G. Luo, and P. H. T. Uhlerr (1995), Yield stress and maximum packing fraction of concentrated suspensions, *Rheol. Acta*, *34*, 544–561, doi:10.1007/BF00712315.

Zou, R. P., J. Q. Xu, C. L. Feng, A. B. Yu, S. Johnston, and N. Standish (2003), Packing of multi sized mixtures of wet coarse spheres, *Powder Technol.*, *130*, 77–83, doi:10.1016/S0032-5910(02)00229-2.